Journal of Molecular Liquids 377 (2023) 121511

Contents lists available at ScienceDirect

Journal of Molecular Liquids

journal homepage: www.elsevier.com/locate/molliq

Light excitation of gold Nanorod-Based hybrid nanoplatforms for simultaneous bimodal phototherapy

Lilia G. Arellano [a,1], Eva M. Villar-Alvarez [b,1], Brenda Velasco [a], Vicente Domínguez-Arca [a], Gerardo Prieto [c], Adriana Cambón [a,*], Silvia Barbosa [a,*], Pablo Taboada [a]

[a] Grupo de Física de Coloides y Polímeros, Departamento de Física de Partículas; Facultad de Física e Instituto de Materiales (iMATUS) e Instituto de Investigaciones Sanitarias (IDIS), Universidade de Santiago de Compostela, 15782 Santiago de Compostela, Spain
[b] Nanostructured Functional Materials Group, Catalan Institute of Nanoscience and Nanotechnology, UAB Campus, 08193 Bellaterra (Barcelona), Spain
[c] Grupo de Biofísica e Interfases, Departamento de Física Aplicada, Facultad de Física e Instituto de Materiales (iMATUS), Universidad de Santiago de Compostela, 15782 Santiago de Compostela, Spain

ARTICLE INFO

Article history:
Received 5 December 2022
Revised 8 February 2023
Accepted 17 February 2023
Available online 24 February 2023

Keywords:
Gold nanorods
Layer by layer
Photodynamic therapy
Isocyanine gree
Phothermal therapy

ABSTRACT

In this work, we developed a hybrid nanosystem able to simultaneously combine its potential as a photodynamic (PDT) and plasmonic photothermal (PPTT) therapeutic agent to kill malignant cells. To do that, AuNRs were functionalized by means of the layer-by-layer (LbL) assembly technique using alternating layers of anionic poly(styrene sulfonate) (PSS) and cationic poly-L-lysine (PLL) as polyelectrolytes (PEs), and an outer final layer of hyaluronic acid (HA) to provide the hybrid particles with both sufficient colloidal stability and targeting ability to tumoral cells overexpressing CD44 receptors. To provide the nanoplatform with PDT capabilities, the near-infrared (NIR) sensitive photosensitizer (PS) indocyanine green (ICG) was previously grafted to the PLL PE and assembled on the particle surface coating; in this manner, PSS/PLL-ICG/HA-coated AuNRs hybrid particles were obtained. Then, the conditions for optimized reactive oxygen species (ROS) production under NIR light excitation were elucidated, reaching ca. 80% after 5 min irradiation at 2.0 W/cm^2 compared to positive control (H_2O_2). Since ICG can also absorb near infrared (NIR) light and transforms it by internal conversion into heat under suitable irradiation conditions, which adds to the photothermal plasmonic effect provided by the metallic NP, the heating profiles provided by the present hybrid nanoparticles (NPs) were measured, being observed temperature increments ranging from 9 to 22 °C. The potential contribution of its different components to both PDT and PPTT were deeply analyzed *in vitro* for intended cancer therapeutics at several power intensities but also at different temperatures with the aim of elucidating the role played by both phototherapies on cell cytotoxicity, the optimal illumination conditions for effective bimodal phototherapy as well as the elucidation of the main cell death mechanism involved. Under optimized conditions and after the administration of 2.5 ·10^{10} NPs/mL, cell cytotoxicites of up to ca. 70% were determined by combination of PDT + PPTT therapeutic effect.

1. Introduction

Plasmonic photothermal therapy (PPTT) is a newly emerging tool to fight against different diseases as cancer which makes use of the outstanding optical properties of plasmonic nanoparticles (NPs). Briefly, PPTT is a minimally-invasive therapeutic strategy in which photon energy is transformed into localized heat leading to sufficient temperature (T) increments in tumoral cells to directly kill them (thermal ablation regime, T > 45 °C) or to sensitize them (thermal sensitization, T < 45 °C) in order to either enhance/complement the therapeutic outcome of an additional first line applied therapy (*i.e.,* radio- or chemotherapy), and/or to induce a suitable cytostatic pathway leading to cell death (*i.e.,* apoptosis). At this respect, Au NPs (*i.e.*, nanospheres, nanorods, nanoshells, nanocages and nanostars) have attracted great attention as potential photothermal agents [1,2] thanks to their high-absorption cross sections for conversion of light into heat. In addition, Au NPs are also known to be biocompatible and, hence, they can be served as nanocarriers for drugs and other bioactive molecules; and their easy surface chemistry allows the attachment of new functionalities as ligands (antibodies, peptides, proteins, etc) for targeted

* Corresponding authors.
E-mail addresses: adriana.cambon.freire@usc.es (A. Cambón), silvia.barbosa@usc.es (S. Barbosa).
[1] **These authors contribute equally to this work**.

https://doi.org/10.1016/j.molliq.2023.121511
0167-7322/

cargo delivery and cell uptake and internalization into tumoral cells [3,4].

Amongst the different types of metallic NPs, gold nanorods (AuNRs) are particularly appealing thanks to their anisotropic structure which allows the electronic oscillations to occur mainly along the short and long axes of the particle resulting in the generation of transverse and longitudinal localized surface plasmon bands (LPSRs) [5,6]. The transversal band is regularly observed in the visible region of the electromagnetic spectrum, whilst the longitudinal one is displayed in the near infrared region (NIR) of the electromagnetic spectrum, which can be easily tuned by modifying the AuNR aspect ratio. AuNRs exhibit the largest NIR absorption cross-section compared to other Au NPs [7], demonstrating an extremely efficient NIR photothermal heat conversion [8,9]. Furthermore, AuNRs possess much larger surface areas per volume than spherical Au NPs, making them an attractive potential nanocarrier with large cargo loading capability, especially useful to co-deliver different types of therapeutical agents to cancer cells [10,11].

While these plasmonic nanostructures can certainly increase the local temperature in cancerous areas upon exposition to NIR light of suitable wavelengths, it is not completely evident that the resulting photothermal effect is enough to achieve the complete eradication of malignant cells while avoiding damage of the surrounding healthy tissue [12,13]. Thus, the development of new nanostructures able to enhance cancer treatment efficacy by the simultaneous combination of different phototherapeutic approaches is vital and can allow to overcome current limitations of single therapies while leading, at the same time, to potential synergistic cytotoxic effects [14–16].

Photodynamic therapy (PDT) is a treatment modality for cancer and other diseases in which targeted cells are selectively destroyed by the biological activity of light-sensitive compounds known as photosensitizers (PSs) [17,18]. When exposed to light of an appropriate wavelength, these PSs become energized and generate reactive oxygen species (ROS) including singlet oxygen ($^1O_2$) to kill cancer cells [18–20]. ROS are naturally generated as a result of the reduction of oxygen during aerobic respiration and by various enzymes within cells. At physiological levels, ROS contribute to cell signaling and host defense mechanisms [21]. Enhanced ROS levels, above the detoxification capacity of a biological system, may result in significant damage of cell structures and oxidative stress, particularly, by means of the alteration of biocromolecules such as polyunsaturated fatty acids in lipid membranes, essential proteins and DNA giving rise to, for example, cell apoptosis [22]. Thus, tumors might be then selectively destroyed by PDT using localized, light-excited PSs avoiding the severe side effects associated with other systemic conventional treatments such as chemotherapy; but also PDT is able re-sensitize cancer cells to chemotherapy through intrinsic regulation of intracellular redox systems, cell death mediators as well as effective activation of immune cells. However, most currently used PSs possess several important disadvantages as their hydrophobic nature, short retention times, and/or poor selectivity to diseased cells and tissues, amongst others. Thus, increasing research efforts are being devoted for developing new potential PSs to overcome the former limitations.

Therefore, PPTT and PDT appear as two photon-mediated therapeutic methods that might be combined in one single nanoplatform for efficient multimodal cancer therapy to achieve simultaneous ROS and hyperthermia-mediated cellular damage [15,23–28]. Hence, with this aim in mind, in this work we developed a hybrid nanoplatform able to simultaneously combine PDT and PPTT therapeutic activities to treat malignant cancer cells. This nanoconstruct was based on surface-functionalized AuNRs by means of the layer-by-layer (LbL) technique using poly(styrene sulfonate), PSS, and poly(L-lysine), PLL, as polymeric coating layers of opposite electric charge. A hyaluronic acid (HA) outer coating layer was deposited onto the NPs to provide the hybrid nanoplatform with active targeting capabilities by exploiting the high affinity of this biopolymer to bind CD44 receptors overexpressed on the membrane surfaces of different tumors as breast, lung and colorectal cancers [29,30]. To provide the platform with PDT capability, the indocyanine green (ICG) dye was also assembled onto the AuNR-surface coating. ICG is a tricarbocyanine compound with absorbing properties in the NIR approved by the US Food and Drug Administration (FDA) for medical diagnostics as a contrast agent for blood volume determination, ophthalmic angiography, cardiac output, and hepatic function [31,32] but also a potential PDT agent for cancer treatment [33,34]. As a consequence of the interaction between metallic nanomaterials and the excited state of fluorophores, free electrons in metals can oscillate with those of fluorophores to produce a dipolar interaction which may result in an enhancement of light absorption, emission, and/or stability of the fluorophore excited state to provide more efficient single PDT and/or combined PPTT and PDT [35–39]. Nevertheless, poor attention has been paid to both identify suitable irradiation conditions for effective either single or dual PDT-PPTT applied therapies for synergistic therapeutic outcomes using multimodal nanoplatforms, and to decipher the predominant cell death mechanism involved in each case. Hence, in this work we also focused on the analysis of the photostability of the encapsulated ICG PS inside the polymeric coating of the nanoplatform, as well as in the role played by illumination conditions on both the NIR-induced temperature heat profiles and ROS production inside tumoral cells. The developed hybrid nanosystem was observed to be an ideally versatile platform to simultaneously deliver localized heat and ROS, whilst providing an efficient protection of the ICG dye molecules to avoid their early clearance from the body. Thus, combined PDT and PPTT may kill cancer cells more efficiently than PDT or hyperthermia treatments alone whereas the predominance of a single or dual therapeutic mode was dependent on illumination and medium conditions, which was reflected both in the cytotoxic response provided as well as in the cell death mechanisms involved.

2. Materials and methods

2.1. Materials.

Hexadecyltrimethyl ammonium bromide for molecular biology (CTAB), tetrachloroauric acid ($HAuCl_4{\cdot}3H_2O$), silver nitrate ($AgNO_3$), sodium borohydride ($NaBH_4$), poly(sodium-4-styrenesulfonate) (PSS) of molecular weight (M_w) ~ 70000 g/mol, poly-L-lysine hydrobromide (PLL) of M_w ~ 22000 g/mol, hyaluronic acid of M_w ~ 15000 g/mol,1,3-diphenylisobenzofuran (DBIPF) and indocyanine green (ICG) were purchased from Sigma-Aldrich (USA). ICG sulfo-NHS ester was from BioActs (Korea). Ascorbic acid was from Fluka. Heat- inactivated fetal bovine serum (FBS), trypsin-EDTA (0.25X) and PBS pH 7.4 (10X) were from Hyclone (Thermo Scientific, USA). Prolong Antifade reagent with DAPI was from Molecular Probes (USA), and the Cell Death Annexin V - Propidium Iodide kit was from Gerbu Biotechnik GmbH (Germany). All other reagents were of analytical grade and/or suitable for cell culture as corresponding. All chemicals were used as received. Milli-Q water (Millipore) was used throughout all the experiments.

2.2. Synthesis of AuNRs.

AuNRs were synthesized using a seed- mediated growth method. First, CTAB-capped Au seeds were obtained. To do that, 7.5 mL of a 0.2 M CTAB solution was gently mixed with 0.25 mL of 0.01 M $HAuCl_4$ in a water bath at 28 °C. As indication, for both

seeds and AuNRs preparation, CTAB was left at a constant temperature of 28 °C for one day under constant stirring of 200 rpm to achieve full solubilization and avoid foaming prior to use. Next, a 0.01 M $NaBH_4$ solution was prepared in ice-cold water. This solution was left to rest for 2–3 min to ensure a good dispersion of the reductant. Afterwards, while the Au-CTAB solution was stirred at 200 rpm, 0.6 mL of ice-cold 0.01 M $NaBH_4$ were added in one pull to the former, after which the mixed solution turned brownish yellow. This solution was mixed gently by hand for 2 min and then left undisturbed in a water bath at 28 °C for 1 h to allow the excess sodium borohydride to be decomposed.

For AuNRs growth, 850 μL of a 0.01 M $HAuCl_4$ solution were added to 20 mL of 0.2 M CTAB in a water bath at 28 °C, after which the solution turned yellow bright while stirred at 500 rpm. Then, 0.01 M of an $AgNO_3$ solution was prepared in darkness. Different volumes of the silver solution (ranging from 126 μL to 246 μL) were added to the Au growth solution followed by gentle mixing at 500 rpm. Then, 136 μL of a 0.1 M ascorbic acid (AA) solution were added followed by gentle stirring at 500 rpm until the solution turned colourless (ca. 4 min). Finally, 220 μL of the Au seed solution were gently added to the Au growth solution while stirring for 2 min and, then, stopped. The resulting solution was left undisturbed in a water bath overnight at 28 °C for ca. 12 h becoming reddish-pink. The formed AuNRs were centrifuged at least twice at 28 °C for 30 min at ca. 29,500 rcf and redispersed in 20 mL of deionized water. The UV– visible absorption spectra of the obtained AuNRs were measured using a Cary Bio 100 UV–vis spectrophotometer (Agilent Technologies, USA). The sizes of the AuNRs were measured using a JEOL JEM 1011 (Japan) transmission electron microscope operating at an accelerating voltage of 120 kVand aspect ratios (ARs) calculated.

The concentration of AuNRs per mL was calculated by means of inductively coupled plasma mass spectroscopy-MS (ICP-MS). For example, for the case of AuNRs with a longitudinal LSPR band centered at 792 nm, 1 mL of three different AuNRs batches at an OD ~ 1 has an Au concentration of ca. 49.2 ± 0.4 μg/mL taking into account the particle length and width obtained by TEM. The final concentration obtained under these conditions was of ca. $5{\cdot}10^{11}$-AuNRs/mL.

2.3. LbL polymeric coating of AuNRs.

Using the LbL methodology, multilayers of PSS, PLL and HA were successfully deposited onto the AuNR surfaces. For the PSS coating, a solution of PSS (10 mg/mL) in 12 mM NaCl (100 mL) was prepared. When this PE was completely dissolved, 1 mL of this solution was mixed with 1 mL of a 12 mM NaCl solution, and the resulting mixture stirred at 500 rpm. Then, 1 mL of an AuNR solution (OD ~ 1) was added dropwise in the PSS solution while stirring. After 1 h of adsorption, the mixture was centrifuged twice at 31,500 rcf for 20 min and resuspended in 1 mL of MilliQ water. Next, a subsequent cationic PLL-ICG layer can be used to coat the hybrids. To do that, a volume of 100 mL of PLL (5 mg/mL) was previously well mixed with a solution containing ICG-sulfo-NHS ester (0.02 mg of ICG, 0.02 mg/mL). The mixture was allowed to react for 2 h at room temperature in the dark, obtaining a PLL-ICG complex by carbodiimide chemistry. Next, to remove unbound ICG, the mixture was dialyzed for 24 h against water with a cellulose dialysis membrane with MWCO of 3500 Da. Then, PSS-coated AuNRs were added dropwise under stirring at 500 rpm. After 1 h of adsorption, the coated metallic NPs were centrifuged at 31,500 rcf for 20 min and resuspended in 1 mL of MilliQ water. The deposition of the final HA layer was made by preparing 60 μL of a HA concentrated solution (1 mg/mL), mixed with 1 mL of MilliQ water and stirred at 500 rpm for 5 min. 1 mL of the former PSS/PLL-ICG-coated AuNRs was added dropwise to the HA solution. After 1 h, the final coated AuNRs were centrifuged at 14,000 rcf for 10 min and redispersed in 1 mL of MilliQ water.

2.4. Nanoplatform characterization

2.4.1. Dynamic light scattering (DLS).

DLS measurements were done using an ALV-5000 digital correlator system (ALV 5000/E, ALV GmbH, Germany) equipped with a temperature control set at 25 °C ± 0.1 °C. The scattered light was vertically polarized with a 532 nm solid-state laser (2 W). The hydrodynamic radius, R_h, was obtained for diluted samples from DLS measurements at an incidence angle of 90° by analysis of the DLS data by means of the CONTIN algorithm [40] and the Stokes-Einstein equation, $R_h = k_BT/6\pi\eta D$, where k_B is the Boltzmann constant, T the temperature, η the solution viscosity, and D the diffusion coefficient of the particles. Measurements were performed at least in triplicate with a sampling time of 60 s each and averaged.

2.4.2. Inductively coupled plasma-mass spectrometry (ICP-MS).

The Au concentration in solution or in cells was determined by inductively coupling plasma mass spectrometry (ICP-MS) in a Varian 820-MS equipment (Agilent Technologies, USA). 1 mL of AuNRs solution (or 100,000 cells with internalized metallic NPs, where corresponding) was dissolved in 0.3 mL HCl 37% (v/v) and 0.1 mL HNO_3 70% (v/v). Solutions were diluted with deionized water until reaching a final volume of 2 mL. The intensity of the emission wavelength was measured and compared to a standard solution.

2.4.3. Electrophoretic mobilities.

Potentials of bare and PE-coated AuNRs were measured using a Nano ZS instrument (Nanoseries, Malvern Instruments, UK) equipped with a 633 nm He-Ne laser of 4 mW. The equipment measures the electrophoretic mobility of the particles and converts it into ζpotential data using the classical Smoluchowski equation:

$$\alpha = \varepsilon\zeta / \eta \tag{1}$$

where α, ε, ζ, and η denote the electrophoretic mobility, permittivity of the medium, the ζpotential of the particles and medium viscosity, respectively. Each sample was fed into a folded capillary, clear, disposable cell. Measurements were initiated after attaining thermal equilibrium at 25 °C. The number of runs for each experimental point was automatically determined by the software, and measurements were performed in triplicate. Results were reported as the mean ± standard deviation (SD). Solution with concentrations lower than 100 $\mu g{\cdot}mL^{-1}$ were used.

2.4.4. Encapsulation efficiency (EE%) of ICG inside the hybrid nanoplatform:

To determine the EE% of ICG within PSS/PLL-ICG/HA-coated AuNRs, the hybrid NPs were centrifuged at 15000 rpm at 20 °C for 20 min. The ICG content in the supernatant was measured by means of fluorescent spectroscopy using a Cary Eclipse spectrophotometer (Agilent Technologies, USA). Previously, a fluorescence calibration curve with free ICG was obtained using light with λ_{ex} = 785 nm and λ_{em} = 810 nm, and the fluorescence of solution supernatants of bare AuNR solutions were also considered as an additional blank. Each sample was measured in triplicate for three different batches. The EE% was calculated by the following expression:

$$EE(\%) = \frac{Total\ amount\ of\ dye\ feeded - dye\ in\ supernatant}{Total\ amount\ of\ dye\ feeded} \times 100 \tag{2}$$

2.4.5. Photostability of ICG assembled onto AuNRs:

The stability of free ICG and PSS/PLL-ICG/HA-coated AuNRs (1 mL, OD ~ 1, ca. $1{\cdot}10^{11}$AuNRs/mL, 22 μM of dye) in water was fol-

lowed for ca. 20 days by measuring their fluorescence decrease. Fluorescence spectra were monitored in a Cary Eclipse spectrophotometer (Agilent Technologies, USA). The excitation was set at λ_{ex} = 785 nm and the emission peak recorded at λ_{em} = 810 nm. Also, the stability under NIR light irradiation was analyzed at several light fluencies (0.5, 1.0, 2.0 W/cm^2). The samples were magnetically stirred and illuminated with NIR-light (808 nm) for a total time of 20 min. The fluorescence spectra were recorded at several times and every experimental point repeated at least three times.

2.5. NIR-laser induced photothermal effect of AuNRs.

Temperature increment tests were performed using a continuous wave fiber-coupled diode laser source of 808 nm wavelength (50 W, Oclaro Inc., San Jose, CA). The laser was powered by a Newport 5700–80 regulated laser diode driver (Newport Corporation, Irvine, CA). A 200-μm-core optical fiber was used to transfer the laser light from the laser unit to the target solution and it additionally was equipped with a lens telescope mounting accessory at the output, which allowed the fine tuning of the laser spot size in the range of 0.1–10 mm. The laser spot size was measured with a laser beam profiler (Newport LBP-1-USB) placed at the same distance (8 cm) between the lens telescope output and the 3 mL cuvette (or the 6-well plate when corresponding), using the software Newport LBP series Measurement Systems v3.11. In this way, the power per unit area was easily obtained. The final spot size was set at 1 cm in diameter. A potentiometer (Newport Optical Power Meter model 1916c) was used to calibrate the output power related to the intensity signal of the laser controller. The temperature of AuNRs samples was measured with a type J thermocouple linked to a digital thermometer inserted into the solutions. Particle solutions were stirred during laser illumination to homogenize the produced heat and ensure that samples were in thermal equilibrium during the entire course of the experiments.

2.6. In vitro ROS generation.

The *in vitro* generation of ROS was performed by following the absorbance decrease at 420 nm of 1,3-diphenylisobenzofurane (DPIBF), which is a specific singlet oxygen trap [41]. Briefly, 1 mL of the corresponding sample (deionized water, free ICG, PSS/PLL/HA-coated AuNRs and PSS/PLL-ICG/HA-coated AuNRs) were placed in a quartz cell, and 100 μL of 1 mM DPIBF in ethanol were added. The concentration of free ICG and ICG bound to PSS/PLL-ICG/HA-coated AuNRs was ca. 22 μM (1 mL, OD ~ 1, ca. $1{\cdot}10^{11}$AuNRs/mL). UV–vis spectra of samples before illumination were recorded and taken as the initial (100%) absorbance value. The sample was magnetically stirred and illuminated with NIR light using a CW-808 nm laser source at different time points. Then, the UV–vis spectra were recorded and the process was repeated twice more. The ROS generation was qualitatively determined at three different laser fluencies: 0.5, 1.0, and 2.0 W/cm^2.

2.7. In vitro ICG release.

Additional stability studies were performed by analyzing the *in vitro* ICG release profiles from the obtained hybrid nanoplatforms at a constant temperature of 37 °C and 300 rpm magnetic stirring for several days. PSS/PLL-ICG/HA-coated AuNRs were incubated at pH 7.4 and pH 5.0 (1 mL, $1{\cdot}10^{11}$AuNRs/mL). To obtain the release profiles, 1 mL of hybrid AuNRs was placed into dialysis tubes (SpectraPore®, MWCO 3500 Da) immersed into 50 mL of buffer supplemented with 10% (v/v) FBS at the pH of interest. The released ICG concentration was determined at different time intervals for each pH solution. At each sampling time, 1 mL of the medium was withdrawn and replaced with the same volume of fresh buffer to maintain the required sink conditions. The ICG content in the supernatant was measured by means of fluorescence spectroscopy using a previously established calibration curve in the corresponding buffer solutions. Fluorescence spectra were monitored in a Cary Eclipse spectrophotometer (Agilent Technologies, USA). Assays were carried out in triplicate.

2.7.1. Protease-assisted release.

To measure the enzymatic release of ICG from AuNRs, 1 mL ($1.0{\cdot}10^{11}$AuNRs/mL) was incubated into dialysis tubes (SpectraPore®, MWCO 3500 Da) at 37 °C under moderate stirring (300 rpm) for several days at pH 7.4 and 5.0 in the absence or presence of trypsin–EDTA (50 μL per 25 mL of buffer) and immersed into 25 mL of buffer supplemented with 10% (v/v) FBS. The released ICG concentrations were determined as explained above.

2.7.2. NIR-light triggered release.

To analyze the effect of laser exposure on ICG release from AuNRs, 1 mL ($1.0{\cdot}10^{11}$ NP/mL), the present hybrid NPs were incubated at 37 °C under moderate stirring (300 rpm) at pH 5.0 inside the dialysis bags as previously commented. The experimental conditions were similar as those previously stated except that AuNRs were exposed to NIR light irradiation of 1.0 and 2.0 W/cm^2 for 5 min after 2, 5, 9, 12 and 48 h of incubation. Irradiation was performed as described above for photothermal experiments.

2.8. Cell cultures.

Cervical HeLa cancer cells and 3 T3 mouse fibroblasts from Cell Biolabs (San Diego, CA) were grown at standard culture conditions (5% CO_2 at 37 °C) in DMEM supplemented with 10% (v/v) FBS, 2 mM L-glutamine, 1% (v/v) penicillin/streptomycin, 1 mM sodium pyruvate, and 0.1 mM MEM non-essential amino acids (NEAA).

2.9. Cellular uptake by fluorescence microscopy.

Cervical HeLa cancer cells were cultured in poly-L-lysine-coated glass coverslips (12 × 12 mm^2) placed inside 6-well plates (2 mL, $1.0{\cdot}10^5$ cells per well) and grown for 24 hat standard culture conditions. Then, the culture medium was discarded. 100 μL of PSS/PLL-ICG/HA-coated AuNRs ($2.5{\cdot}10^{10}$AuNRs/mL) were redispersed in cell culture medium with 10% (v/v) FBS and added. After 6 h of incubation, the NP containing cells were washed three times with PBS pH 7.4, and then fixed with paraformaldehyde 4% (w/v) for 10 min, washed with PBS, permeabilized with 0.2% (w/v) Triton X-100, and stained with BODIPY Phalloidin. Cells were washed again with PBS, mounted on glass slides stained with DAPI, and cured for 24 h at −20 °C. Samples were visualized with a 63X (oil-immersion, NA 1.4) objective using a confocal spectral microscope Leica TCS-SP2 (LEICA Microsystems Heidelberg GmbH, Mannheim, Germany), whereby the blue channel corresponds to DAPI (λ_{ex} = 355 nm), the pink channel to BODIPY Phalloidin (λ_{ex} = 633 nm) and transmitted light to differential interference contrast (DIC)-mode. Green channel corresponds to the reflected light emitted by the nanoplatform.

2.10. Fluorescence microscopy ROS assay in tumoral cells.

A fluorometric intracellular ROS kit (Sigma-Aldrich, USA) was used to detect ROS according to manufacturer's instruction. Briefly, $1.0{\cdot}10^5$ HeLa cells/well were seeded on 6-wellplates with 2 mL of DMEM without red phenol and grown for 24 h at standard culture conditions. Afterwards, 500 μL of PSS/PLL-ICG/HA-coated AuNRs at a concentration of $2.5{\cdot}10^{10}$AuNRs/mL were added to the wells and incubated for 6 h. Then, the medium was discarded, cells were washed three times with PBS and, finally, fresh culture medium

without red phenol was added. Then, 100 μL of ROS detection reagent were added to each well and cells were incubated for 1 h at 37 °C. Next, cells were treated with a CW diode laser (808 nm) at 1.0 W/cm^2 for 5, 10 or 15 min. As a negative control some cells were left untreated (without NPs), and as a positive control 100% ROS was induced by adding in this step H_2O_2 (800 μM, 33% (w/v)). Then, cells were left in the incubator other 30 min. Samples with live cells were visualized at 20X using an inverted wide field and fluorescent microscopy (Leica DMI6000B, Leica Microsystems, Germany) using the green channel for ROS fluorescence signal (λ_{ex} = 490 nm/λ_{em} = 520 nm), and the transmitted light in differential interference contrast (DIC) mode.

2.11. In vitro cell cytotoxicity.

Cytotoxicity of PSS/PLL-ICG/HA-coated AuNRs was tested *in vitro* by means of the CCK-8 cytotoxicity assay. Cancerous cervical HeLa and 3 T3 Balb fibroblasts cells were seeded into 96-well plates ($1.0{\cdot}10^4$ cells/well) and grown for 24 h at an optical confluence of 80–90% under standard culture conditions in 100 μL growth medium. PSS/PLL/HA-coated AuNRs, PSS/PLL-ICG/HA-coated AuNRs and free ICG were used as negative and positive controls, respectively. After 24 h of incubation at 37 °C, 100 μL of NPs at $2.5{\cdot}10^{10}$ NP/mL in the corresponding cell culture medium were injected into the wells and incubated for 24 h and 48 h. Some wells were tested in the absence of NPs as a negative control (blank), and with free ICG at the same concentration as that encapsulated in the hybrid AuNR nanoplatform. After incubation, the culture medium was discarded, cells were washed with 10 mM PBS (pH 7.4) several times, and fresh culture medium (100 μL) containing 10 μL of CCK-8 reagent added to each well. After 2 h, the absorption at 450 nm of cell samples was measured with an UV–vis microplate absorbance reader (Bio-Rad model 689, USA). Cell viability (SR, survival rate) was calculated as follows:

$$SR = \frac{Abs_{sample}}{Abs_{blank}} \times 100 \quad (3)$$

where Abs_{sample} is the absorbance at 450 nm for cell samples, and Abs_{blank} is the absorbance corresponding to the sample controls without the particles. In addition, some of the wells were also irradiated with a continuous wave fiber-coupled diode laser source at 808 nm (50 W, Oclaro, Inc., San Jose, CA). The used power fluencies were 0.5, 1.0, and 2.0 W/cm^2 for 5 min. After 18 h and 42 h, cells were washed again, and new fresh culture medium (100 μL) was added with 10 μL of CCK-8 reagent to each well and measured as specified above. Experiments were repeated at least three times.

2.12. Statistical analysis

Statistical analysis of experimental data was performed with Origin software. All results were presented as mean standard deviation unless otherwise stated. One-way ANOVA (*P < 0.05; **P < 0.01) was used to determine statistical differences for multiple groups, whereas unpaired *t*-test was used to analyzed individual groups.

3. Results and discussion

3.1. Synthesis and characterization of PSS/PLL-ICG/HA AuNRs nanoplatforms

Bare AuNRs were prepared by means of a well-established two-step seed-mediated growth method with slight modifications [13]. The obtained anisotropic metallic NPs exhibited a size of ca. 33 × 9 nm with two absorption bands: a weak shorter transversal plasmon band at ca. 512 nm and a stronger longitudinal one at ca. 792 nm, respectively. To mask the remaining CTAB molecules adhered to the NPs surface after the synthesis and subsequent washing steps, which are potentially toxic to cells and tissues and provide the metallic particles with colloidal stability, particleś surfaces were modified through the layer-by-layer (LbL) self-assembly technique. Hence, sequential layers of anionic PSS, cationic ICG-modified PLL, and anionic HA polymers were alternatively deposited onto the surface of NPs to give PSS/PLL-ICG/HA-coated AuNRs. The outer HA layer was incorporated to reduce the total positive surface electrical charge of the nanoplatform in order to avoid potential cell toxic effects due to excessive surface positive electric charge as well as allowing specific targeting to CD44 receptors commonly overexpressed in the cytoplasmatic membrane of several types of malignant stem and cancerous cells, as previously mentioned [42,43]. To provide the nanoplatform with PDT and optical imaging capabilities, the cationic PLL polymer was conjugated with ICG molecules by carbodiimide chemistry. The efficiency of ICG complexation with PLL was ca. 94% and the degree of substituted PLL amino groups with ICG was 0.1%, which does not interfere with the cationic charge of the PE in the LbL self-assembly procedure.

Fig. 1a-b shows the main physico-chemical characteristics of the obtained PSS/PLL-ICG/HA-coated AuNRs. The transverse plasmon peak located at ca. 512 nm almost remained invariable as the consecutive layers containing PSS, PLL-ICG and HA were deposited onto the metallic NPs. In contrast, the longitudinal LSPR band changed upon PE deposition as a consequence of the sensitivity of the metallic NPs to the dielectric properties of the surrounding environment [44,45]. This confirmed the successful surface polymeric coating. The initial blue-shift of the LPSR band after PSS deposition may be related to the lower refractive index (RI) of this PE compared to that of CTAB (1.43 *vs.* 1.38) [46]. Conversely, the opposite trend, that is, a red shift of the LPSR maximum, was noted when adsorbing the PLL-ICG polymer conjugate (RI of PLL = 1.52). A certain broadening of the LPSR peak after the final HA layer was observed which is probably related to the formation of some particle clusters, as seen in TEM images (Fig. 1f-g). The successful presence of the ICG dye within the particle coating was additionally confirmed by the development of a shoulder at ca. 745–750 cm^{-1} and a maximum at ca. 804 nm, which is slightly shifted regarding the two characteristic absorption peaks of this PS located at the NIR window at the measured conditions, one at 720 nm (oligomeric form) and another at 820 nm (monomers) [47], respectively.

ζ-potential and FTIR data also confirmed the successful coverage of AuNRs by the PE layers. A complete surface charge reversal after coating the particles with PSS and PLL-ICG conjugate was observed as consequence of their different electrical charge (Fig. 1c). For HA, we controlled its deposition to obtain slightly positively charged particles, which should be relatively more effective in being uptaken by negatively charged cells [48], as mentioned previously. Fig. 1d shows that the FTIR spectrum of PSS/PLL-coated AuNRs displayed bands at 1236 cm^{-1} belonging to C-N stretching, at 1545 and 1639 cm^{-1} corresponding to NH_2 bending and C = O stretching of PSS, 2948 cm^1 to asymmetric C–H stretching, and finally, at 3415 cm^{-1} for symmetric NH_2 and O–H stretchings, respectively. Meanwhile, the FTIR spectrum of free ICG confirmed the presence of characteristic vibrational modes at 883, 1277, 1409, 2923 and 3460 cm^{-1} corresponding to N–H torsion, C-O, C-N and C = C stretchings, C–H bending and N–H symmetric stretching, respectively. The presence of ICG within PSS/PLL-ICG/HA-coated AuNRs was reflected by the development of peaks at ca. 1407 and 1280 cm^{-1} corresponding to C-N stretching and C = C vibrations of the PS aromatic rings. Finally, the HA coating was confirmed by the development of additional peaks at ca.

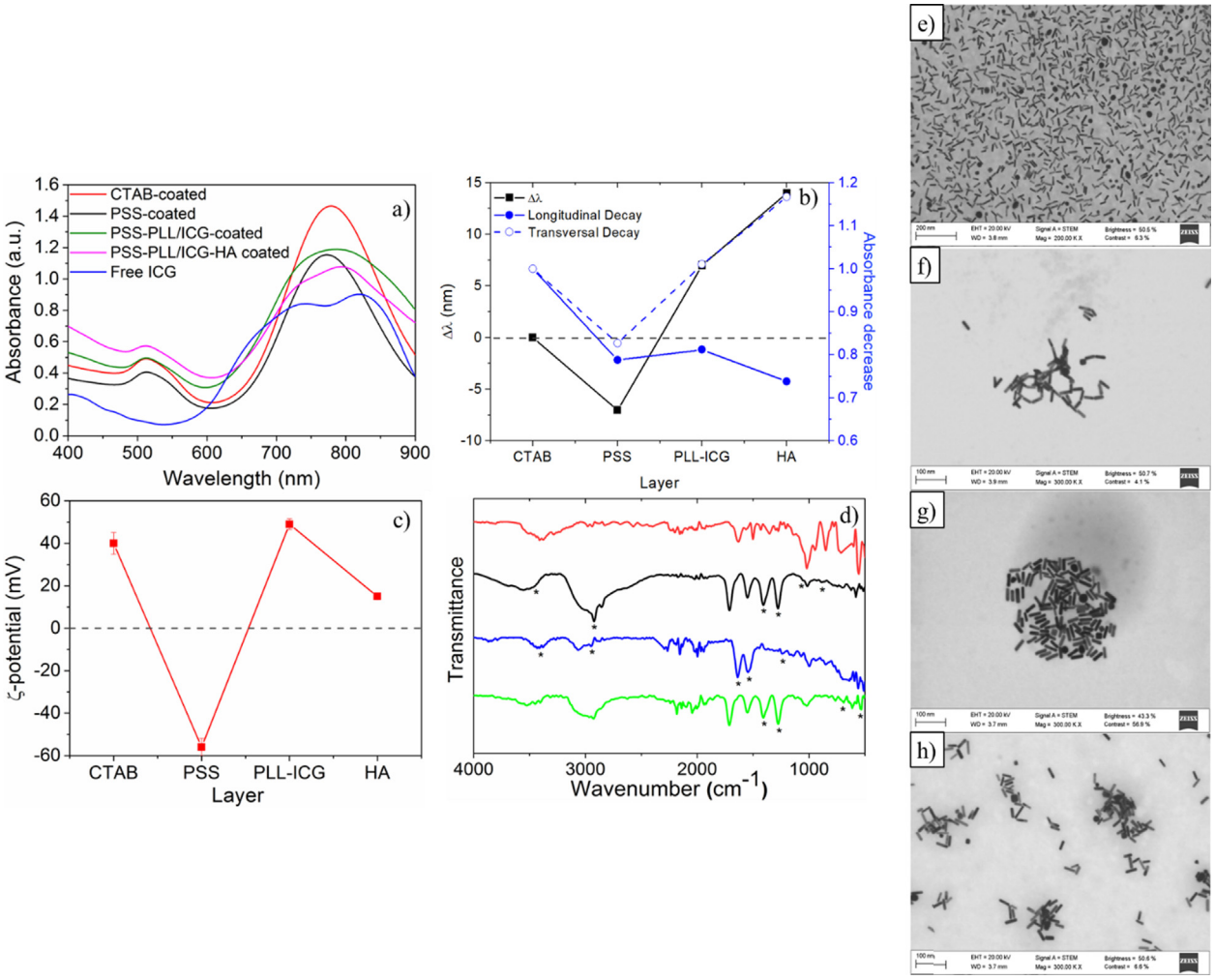

Fig. 1. (a) UV–vis absorbance spectra of PSS/PLL-ICG/HA-coated AuNRs after each coating deposition step. Some physical properties for the nanoplatform are also shown: b) Longitudinal LSPR shifts (■), absorbance decreases from the longitudinal (●) and transversal modes (◯); and c) ζ-potentials. Solid and dashed lines are only to guide the eye. d) FTIR spectra of CTAB-coated AuNRs (——), free ICG (—), PSS/PLL coated AuNRs (——) and PSS/PLL-ICG/HA coated AuNRs (——). TEM images of e) CTAB-coated AuNRs; f) PSS-coated AuNRs; g) PSS/PLL-ICG-coated AuNRs; and h) PSS/PLL-ICG/HA-coated AuNRs. Asterisks in d) indicated the main peaks discussed in the text.

769 cm^{-1} and 545 cm^{-1} assigned to C-O stretching vibrations and α-glycosidic linkages and O–H extensions, respectively.

3.2. Photo- and chemical stabilities of PSS/PLL-ICG/HA-coated AuNRs

As commented previously, ICG is a water-soluble tricarbocyanine dye that strongly absorbs and emits light in the NIR region of the electromagnetic spectrum. However, for intended biomedical applications it is necessary to carefully consider the NIR light dose to be applied to maximise ROS and/or heat generation while precluding dye photodegradation and thermal decomposition as a consequence of temperature increases from non-radiative thermal decays [49–54]. For these reasons, the photostability of free ICG and PSS/PLL-ICG/HA-coated AuNRs was compared for ca. 20 days in the absence and presence of NIR light illumination. Fig. 2a, shows that the stability of the fluorescence signal from ICG complexed to AuNRs was enhanced compared to that of free ICG at similar concentration (22 μM, 84% dye encapsulation efficiency within the nanoplatform) in the absence of light excitation. An initial fluorescence intensity reduction of ca. 15% was noted for PSS/PLL-ICG/HA-coated AuNRs after 2 days of incubation, much lower than 70% detected for the free ICG dye; after one week, additional reductions of ca. 20 and 15% of the fluorescence signals were observed, respectively, with no further decreases observed at longer incubation times [50].

Conversely, the photostability of both free ICG and PSS/PLL-ICG/HA-coated AuNRs was reduced after their NIR light excitation, and such destabilization was more important as the fluence increased: For PSS/PLL-ICG/HA-coated AuNRs the observed fluorescence reduction was ca. 28%, 25% and 14% after 15 min of NIR illumination at 2.0, 1.0 and 0.5 W/cm^2, respectively, which was rather similar to that obtained, for example, with other types of anisotropic gold nanoparticles as nanoshells, in which ICG was entrapped inside the polymeric core [55]. It was clearly observed that the conjugation of the dye to the PLL polymer and subsequent integration into the nanoplatform surface coating enhanced the photochemical protection of ICG, as confirmed by comparison with the strong loss of fluorescence signal of the free ICG dye (ca. 44%) after 15 min of NIR laser irradiation at 2.0 W/cm^2 (Fig. 2b). In summary, the present observations evidenced that the dye-PE complex conjugated to the hybrid nanoplatform was relatively stable upon continuous wave (CW) laser illumination at the selected NIR irradiation durations and fluencies.

To analyze the protection provided by the AuNR-based platform to the conjugated ICG dye under relevant physiological conditions, ICG release profiles at both neutral and acidic conditions (pH 7.4

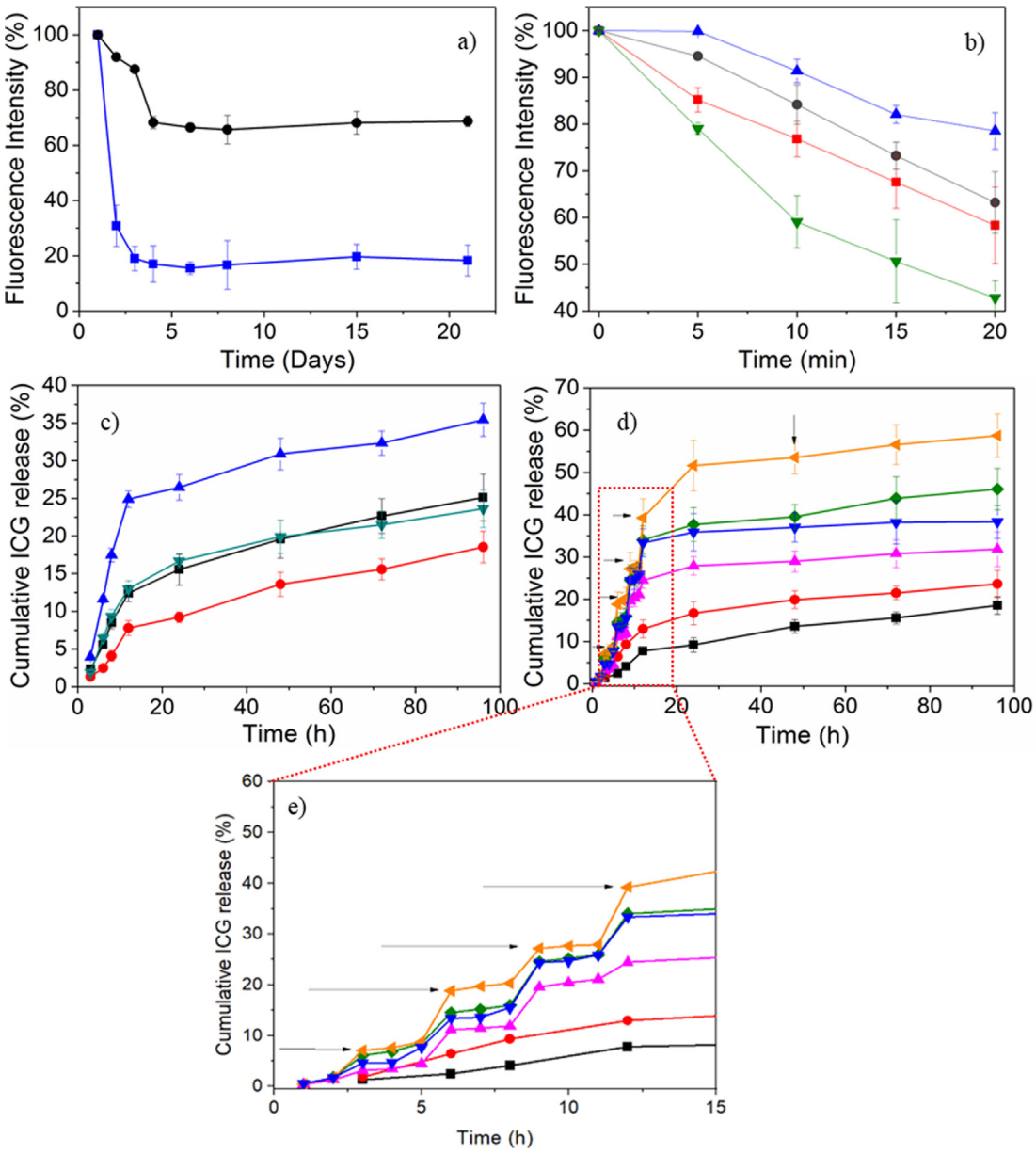

Fig. 2. (a) Time evolution of fluorescence intensity of free ICG (■) and PSS/PLL-ICG/HA-coated AuNRs (●). (b) Photostability of PSS/PLL-ICG/HA-coated AuNRs under continuous illumination with NIR light of 2.0 (■), 1.0 (●) and (▲) 0.5 W/cm^2. Fluorescence intensity of free ICG at the maximum fluence is also shown for comparison (▼). Lines are only to guide the eye. c) ICG cumulative releases from PSS/PLL-ICG/HA coated-AuNRs in the absence (●,▼) and presence (■,▲) of trypsin at pH 5.0 (●, ■) and 7.4 (▼, ▲), respectively. d) ICG cumulative release from PSS/PLL-ICG/HA-coated AuNRs at pH 5.0 in the absence of trypsin and NIR light (■), in the presence of trypsin (●), in the presence of NIR illumination at 1.0 (▲) and 2.0 (◆) W/cm^2, and the simultaneous presence of both trypsin and NIR light irradiation at 1.0 (▼) and 2.0 (▼) W/cm^2 provided by a laser source of 808 nm (for 5 min), respectively. e) Zoom of the initial release area showing the stair-like release profile of the dye upon NIR illumination. Lines are only to guide the eye. Arrows denote the time points of irradiations: 2, 5, 9, 12 and 48 h. Measurements were performed in triplicate (n = 3).

and 5.0) in the presence of 10% (v/v) FBS were monitored for 96 h at 37 °C. Moreover, the influence of both endogenous (the protease trypsin) and exogenous (NIR light) triggers to induce ICG release were also considered. In vitro cumulative ICG release profiles at both neutral (pH 7.4) and acidic conditions (5.0, mimicking lysosomal pH) showed a burst phase followed by a much slower diffusion release pattern.

The release profiles were slightly faster and larger in the presence of trypsin, as expected by the protease-induced PLL degradation [56], -ca. 26% and 40% at pH 5.0 and 7.4 compared to ca. 20% and 32% in the absence of the enzyme after 96 h of incubation, respectively, see Fig. 2c. However, the final release extents were low since amide bonding upon ICG conjugation to PLL hinders a massive diffusion of the PS out of the coating layer despite the progressive degradation of the PLL polymer by trypsin. This was especially noted at acidic pH, in which the PLL ($pK_a \approx 9–10$) layer electrostatically interacts with the underlying PSS chains ($pK_a \approx 1–2$) even in the presence of the enzyme compacting the PE coating and, thus, offering protection to avoid excessive dye diffusion out of the nanoplatform.

On the other hand, when applying 808 nm CW NIR laser irradiation at 1.0 and 2.0 W/cm^2 for 5 min after 2, 5, 9, 12, and 48 h of incubation, ICG release extents at pH 5.0 after 96 h,were ca. 32 and 38%, respectively, values slightly larger than in the presence of the enzyme (Fig. 2d). It is worth mentioning that light-induced releases were characterized by a stair-like profile, that is, a strong

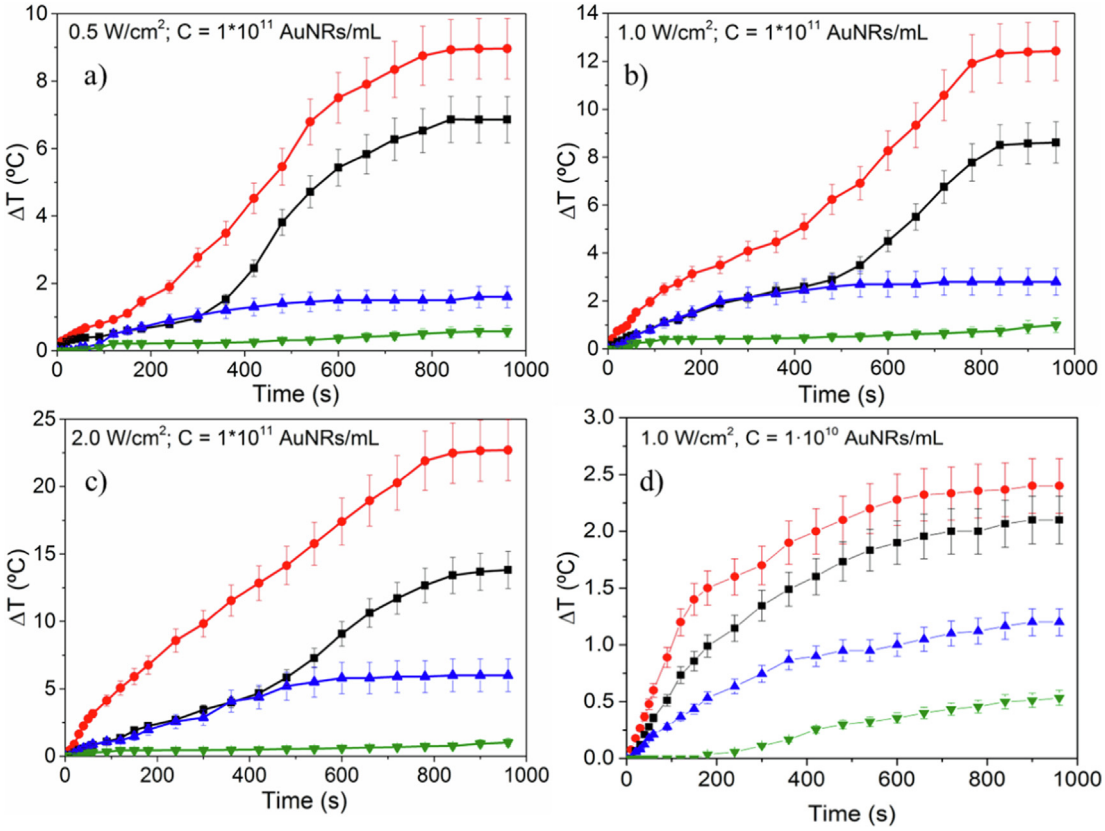

Fig. 3. Temperature increases along incubation under NIR light irradiation (808 nm). Three power intensities were tested: 0.5 W/cm^2 (a), 1.0 (b) and 2.0 W/cm^2 at two nanoplatform concentrations $1{\cdot}10^{11}$ NPs/mL (a-c) and $1{\cdot}10^{10}$ NPs/mL at 1.0 W/cm^2 (d) for (■) PSS/PLL-ICG/HA-coated AuNRs, (●) PSS/PLL/HA-coated AuNRs, (▲) free ICG (equivalent concentration to that loaded inside PSS/PLL-ICG/HA-coated AuNRs), and (▼) pure aqueous solution. Measurements were performed in triplicate (n = 3).

burst phase just right after the application of the light external stimulus followed by a progressive levelling off at longer times. This provides an excellent control over the cargo release kinetics on demand.

Moreover, the combination of both internal (enzyme) and external (light) stimuli enhanced the release rate compared to the application of individual stimuli, with up to ca. 46 and 59% of entrapped ICG being released under 1.0 and 2.0 W/cm^2 NIR light irradiation + trypsin at pH 5.0, respectively, which are much higher if compared with quantities detected after the application of the individual NIR light (32 and 38%, respectively) or trypsin triggers (24% under both conditions).

3.3. NIR-induced temperature heat profiles of PSS/PLL-ICG/HA-coated AuNRs

As shown in Fig. 1, the ICG absorption spectrum when the dye is bound to the nanoplatform showed a shoulder at ca. 745–750 nm and a maximum at ca. 802 nm, as mentioned previously. After light absorption, an ICG molecule can follow three different pathways to deactivate its excited state [57]: i) The absorbed energy can be converted into heat by internal conversion mechanisms (ca. 80–85 %) [58]; ii) the absorbed energy can be emitted as fluorescence light [32]; iii) part of the absorbed light is transferred to the ICG triplet T_1 state, which enables the generation of ROS when relaxed to the forbidden singlet state [59]; Therefore, heat generation is also a major process after light absorption by ICG (extinction coefficient, $\varepsilon_{ICG} = 1.1{\cdot}10^4$ M^{-1}cm^{-1} at 778 nm), and which is added to the heat-to-light conversion induced by the metallic core (AuNR) of nanoplatforms ($\varepsilon_{AuNR} = 2.0{\cdot}10^9 \pm 0.1{\cdot}10^9$ M^{-1}cm^{-1}). Then, it appears necessary to analyze the nature of the coupled light-to-heat conversion in PSS/PLL-ICG/HA-coated AuNRs provided by the metallic core and ICG dye in order to elucidate whether there exists a competitive or synergistic effect for light-induced heat production. The light-triggered temperature increments under 808 nm NIR light irradiation of PSS/PLL-ICG/HA-coated AuNRs, PSS/PLL/HA-coated AuNRs, and free ICG were obtained at three laser fluencies (0.5, 1.0, 2.0 W/cm^2) and two particle concentrations ($1{\cdot}10^{11}$ and $1{\cdot}10^{10}$ NP/mL). Free ICG concentrations of 22 and 2.2 μM, respectively, similar as those present in AuNR-based nanoplatforms, were used as controls.

Pure aqueous solutions increased their temperature<1 °C under any irradiation condition along the time interval tested. Conversely, temperature increments provided by free ICG (at 22 μM) were ca. 1.6, 2.8 and 6.0 ^{0}C under 0.5, 1.0 and 2.0 W/cm^2, respectively, which confirms the effective capacity of this dye to convert light into heat [58–61]. For the nanoplatforms, either PSS/PLL/HA-coated or PSS/PLL-ICG/HA-coated AuNRs, particle and fluence dependences of the reached solution temperatures were clearly observed. Strong temperature increases of up to 22.6 and 13.8 ^{0}C were observed for PSS/PLL/HA-coated and PSS/PLL-ICG/HA-coated AuNRs under irradiation of 2.0 W/cm^2 at a particle concentration of $1.0{\cdot}10^{11}$ NPs/mL, respectively, with a temperature maximum after 15 min which does not further change. Similar temperature increments were also obtained for other types of anisotropic nanoparticles as Au nanoshells [55] or nanoprisms [62]. As commented previously, this increment stem from the excitation of the dye to their triplet state and subsequent relaxation to the singlet one, but also to the relaxation of Au metal hot electrons and subsequent energy transfer upon their relaxation to the crystal lattice of the metallic core, which further relaxes through heat emission [23,44]. When decreasing the particle concentration to

$1.0{\cdot}10^{10}$ NP/mL, the observed temperature increase was rather lower, ca. 2.4 and 2.1 ^{0}C, respectively, and with a maximum detected after ca. 10–12 min of irradiation. In addition, by comparing PSS/PLL-ICG/HA-coated AuNRs and their PSS/PLL/HA-coated counterparts lower temperature enhancements were observed for the former, and these differences were generally larger as the fluence increased. Such observations might stem from the ability of ICG to absorb NIR light, thus, competing with the light-to-heat metal NP conversion. In the former case, after light absorption ICG returns to its ground state through fluorescent radiative decay, singlet oxygen production and/or by internal conversion (non-radiative decay) with heat emission, being then a less efficient photothermal agent than the metal NPs. It is also known that absorption cross section of Au NPs is orders of magnitude stronger than that of most strongly absorbing molecules [13]. In this case, the molar extinction coefficient of AuNRs obtained was ca. $\varepsilon = 2.10^{9} \pm 1.10^{9}$ $M^{-1}cm^{-1}$, in agreement with previous data [63]. This value is 5 orders of magnitude larger than the molar extinction coefficient of ICG ($\varepsilon = 1.08 \times 10^{4}$ M^{-1} cm^{-1} at 778 nm), so that the energy absorbed by the dye is not converted into heat so efficiently as in the case of metal AuNRs cores [64]. Hence, the observed temperature increments in the presence of the dye within the polymeric coating of Au NRs were lower, [26]; on the other hand, part of the incident energy can be also transmitted to PE layers decreasing the heat conversion efficiency. Despite the PEs used herein do not absorb at NIR frequencies hot electrons produced by the longitudinal plasmon decay might be transferred to the wrapped PEs [65].

3.4. In vitro singlet oxygen generation

The possibility of using the PSS/PLL-ICG/HA-coated AuNR nanoplatform as a potential PDT agent was tested by measuring its $^{1}O_2$ generation capability under NIR laser irradiation at 808 nm. The generation of $^{1}O_2$ was quantitatively determined by following the absorbance intensity decrease of the DPIBF probe at 420 nm, which is a specific singlet oxygen trap, at different time intervals [66].

$^{1}O_2$ production was observed to increase (DPIBF absorbance decreases) after 30 min of continuous laser irradiation (Fig. 4d), which certainly indicated that an effective reduction in the $^{1}O_2$ production took place. Also, this was enhanced as the irradiating energy input did (Fig. 4a-d). Interestingly, the $^{1}O_2$ generation by PSS/PLL-ICG/HA-coated AuNRs was slightly lower than that of free ICG at similar concentrations since the effective laser energy available for $^{1}O_2$ production was lower in the former case. For the nanohybrid platform, the laser energy was simultaneously absorbed by the dye and the metal core to produce both singlet oxygen species and heat, and the accessibility of the dye to the oxygen dissolved in the aqueous solution medium was also more reduced since the PS is inside the polymeric coating [15,67,68]. It is also worth mentioning that pure aqueous solution and PSS/PLL/HA-coated AuNRs also led to certain transformation of DIPBF, as noted by slight decreases in its absorbance. This effect stemmed from the nature of the primary oxidation product of DPIBF, an unstable ozonide which cleaves into a dibenzoylbenzene plus an unknown oxygenated product under continuous NIR light irradiation in aqueous environment [69–71]. Both samples exhibited the same absorbance reductions since they did not truly generate $^{1}O_2$ by themselves, so they can be used as references of the DPIBF degradation process.

3.5. In vitro ROS assay in tumoral cells

The capacity of PSS/PLL-ICG/HA-coated AuNRs as potential intracellular PDT agent was next evaluated. As a first step, the successful uptake of the hybrid nanoplatform by HeLa cells after 6 h of incubation was confirmed by both TEM and epifluorescence microscopy images (Fig. 4e-g and Fig. 5). TEM images confirmed the incorporation of the NPs inside the cell cytoplasm within endosomes (Fig. 4e-g), with a perimembrane location. Moreover, light reflected by the metal-core hybrid NPs also denoted that these were present inside cells in the form of small aggregates. In addition, the *in vitro* ROS production by PSS/PLL-ICG/HA-coated AuNRs under 808 nm NIR laser illumination of 1.0 W/cm^2 was qualitatively evaluated at different time intervals by epifluorescence microscopy (λ_{ex} = 490 nm/λ_{em} = 520 nm) in cancerous cervical HeLa cells by means of a fluorometric assay (see Experimental Section for details). Untreated HeLa cells were used as the negative control, and cells supplemented with H_2O_2 (800 μM) as the positive one. Fig. 5 shows that green fluorescence signal and, hence, ROS production increased as the irradiation time was longer. Untreated cells did not show any fluorescence signal as expected, whereas some scarce background signal was also detected when the nanoplatform was internalized into cells in the absence of NIR illumination due to either some metabolic stress generated by uptake (in agreement with toxicity data, see below) and/or the existence of some light reflection from the nanoplatforms themselves.

On the other hand, a relative measure of ROS production after 6 and 24 h of incubation at fluencies of 1.0 and 2.0 W/cm^2 (808 NIR light) for 5 and 10 min of irradiation at different solution temperatures (4, 25 and 37 °C) was additionally performed using a plate reader. The temperature dependent production of ROS was here considered in order to decouple the potential contributions from photodynamic and photothermal responses to cell cytotoxicity (see below for details). Untreated and H_2O_2-treated cells were used as the negative and positive controls, respectively. An additional control consisting of PSS/PLL/HA-coated AuNRs was also considered.

Fig. 6a shows that the fluorescence signal denoting the presence of ROS was enhanced at a fluence of 2.0 W/cm^2 with ca. 78–80%, much larger that 57–59% obtained under to 1.0 W/cm^2 after 5 min of irradiation, compared to the positive H_2O_2 control (100%). No significant effects of the macroscopic solution temperature on ROS generation were observed. ROS production was also more important as the irradiation time was extended up to 10 min (Fig. 6b), with values of ca. 69–71% and 82–84% at 1.0 and 2.0 W/cm^2, respectively. Finally, it is clearly observed that ROS generation decreased with incubation time as expected, being a consequence of both cell death (see below) upon light exposition and the progressive relaxation of the excited dye to the ground state, thus, reducing ROS generation.

3.6. In vitro therapeutic activity in tumoral cells

The therapeutic activity of the PSS/PLL-ICG/HA-coated AuNR platform was assessed by means of the CCK-8 proliferation assay at three different temperatures, 4, 25, and 37 °C at different NIR fluencies (1.0 and 2.0 W/cm^2), incubation (6 and 24 h) and irradiation times (5 and 10 min) in cervical cancerous HeLa cells in order to identify the origin of the cytotoxic response of the platform under light excitation and the existence or not of potential therapeutic synergistic/additive effects under dual PDT/PPTT bi-therapy.

Fig. 7a shows that under 1.0 W/cm^2 NIR light irradiation for 5 min, the PSS/PLL/HA-coated AuNR platform hardly provides a photothermal therapeutic effect except at 37 °C, for which cell toxicity reaches ca. 18%; for this solution temperature, the thermal increment (ca. 2–3 ^{0}C, see Fig. 3) is enough to achieve certain cell sensitization leading to the beginning of apoptosis, as previously reported [10,72]. Such an effect is enhanced when the incubation time is extended up to 24 h, reaching ca. 35% cell death.

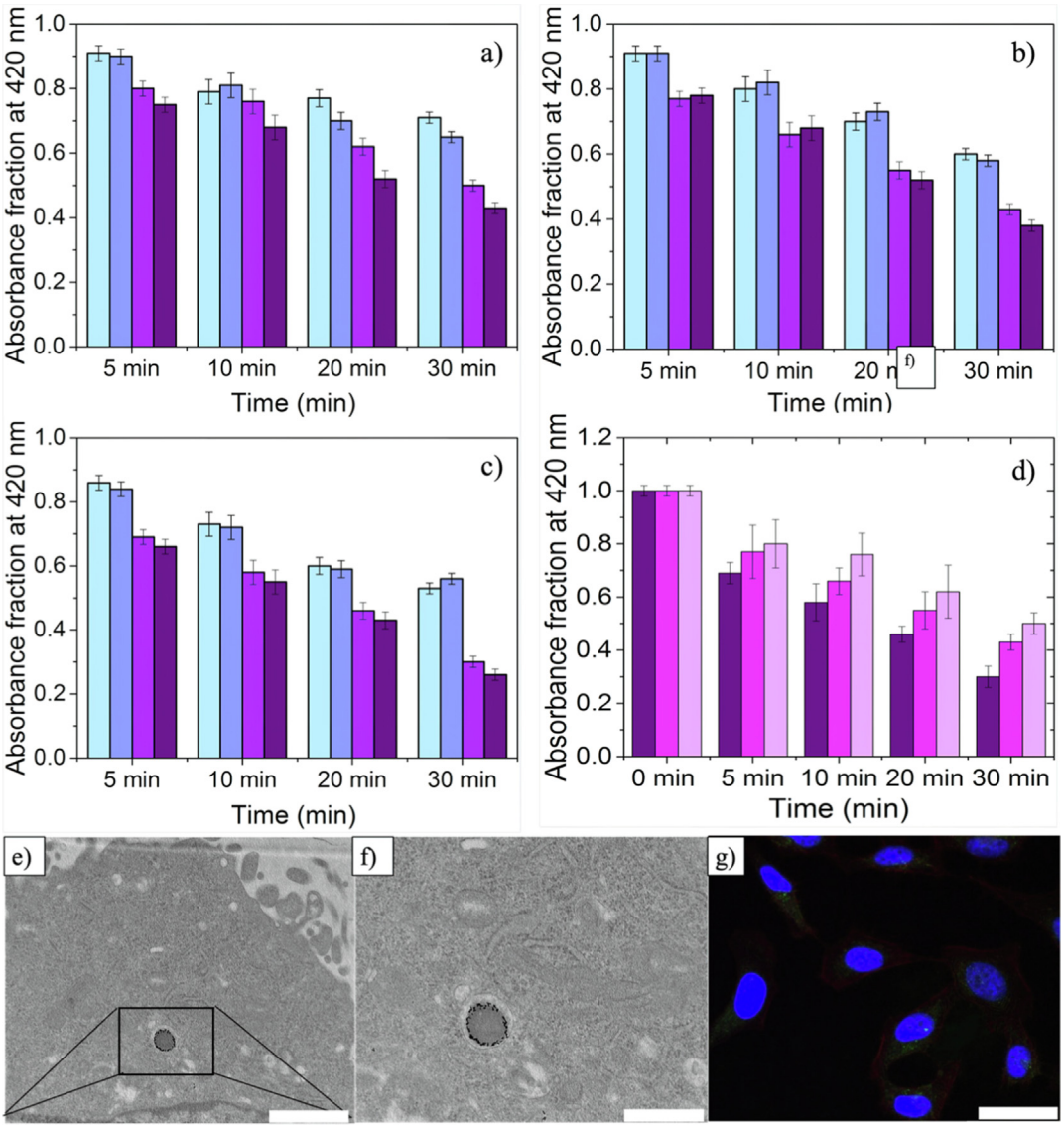

Fig. 4. Quantification of $^1O_2$ production through the DPIBF absorbance decrease at 420 nm in pure aqueous solution (——), or in thre presence of PSS/PLL/HA-coated AuNRs (——), free ICG free (——) and PSS/PLL-ICG/HA-coated AuNRs (——) at (a) 2.0, (b) 1.0, and (c) 0.5 W/cm^2. (d) Comparison of $^1O_2$ production for PSS/PLL-ICG/HA-coated AuNRs illuminated for 30 min at 2.0 (——), 1.0 (——), and 0.5 (——) W/cm^2. e) TEM image of PSS/PLL-ICG/HA-coated AuNRs internalized within an endosome of a HeLa cell; f) zoomed TEM image; and g) confocal image of PSS/PLL-ICG/HA-coated AuNRs in reflection mode inside HeLa cells. Nuclei are stained with DAPI. Scale bars 1 μm. In (a-d), measurements were performed in triplicate (n = 3).

Conversely, when incorporating the ICG dye within the hybrid nanostructure (PSS/PLL-ICG/HA-coated AuNRs), cell toxicity increases up to ca. 29–30% in the temperature range 4–25 ^{0}C and to ca. 35% at 37 ^{0}C after 6 h of incubation, with further increments to 35% and ca. 43% after 24 h of incubation, respectively. These data confirm then that the encapsulation of ICG promoted the generation of ROS species under NIR illumination, as confirmed by the observed enhancement in cell toxicity at 4 and 25 $^\circ$C for PSS/PLL-ICG/HA-coated AuNRs compared to PSS/PLL/HA-coated ones. Here, it is necessary also to remind that the macroscopic temperature increments provided by the PSS/PLL-ICG/HA-coated AuNRs are lower than those of PSS/PLL/HA-coated ones, so the observed toxicity enhancement cannot be from thermal origin. On the other hand, free ICG dye provided cell mortalities between 30 and 35% and 45–50% after 6 and 24 h of incubation, respectively, rather similar as those of the PSS/PLL-ICG/HA-coated AuNR platform. It is also worth mentioning that toxicity by ROS generated from the addition of H_2O_2 to cells and used as control was very large and within 64–68%.

When increasing the irradiation fluence to 2.0 W/cm^2 for 5 min, an additional enhancement of cell toxicity promoted by the PSS/PLL/HA-coated AuNR platform was observed, which is more relevant after 24 h of incubation and at the highest incubation temperature tested (37 ^{0}C, see Fig. 7b). At 4 and 25 ^{0}C ROS production and, thus PDT, seemed the main contribution to cell death, with cell toxicities lying within the range of 40–44% and 49–54% for PSS/PLL-ICG/HA-coated AuNRs after 6 and 24 h of incubation, respectively. Conversely, cell mortalities were ca. 23 and 50% and 42 and 61 % for PSS/PLL/HA-coated and PSS/PLL-ICG/HA-coated AuNRs after 6 and 24 h of incubation, respectively, at 37 °C. Then, it seems that as the fluence increases the contribution of the photothermal effect to cell death became stronger at the largest incubation temperature by allowing to reach a stronger sensitization or even the cell ablation regime. In this regard, similar observations were also

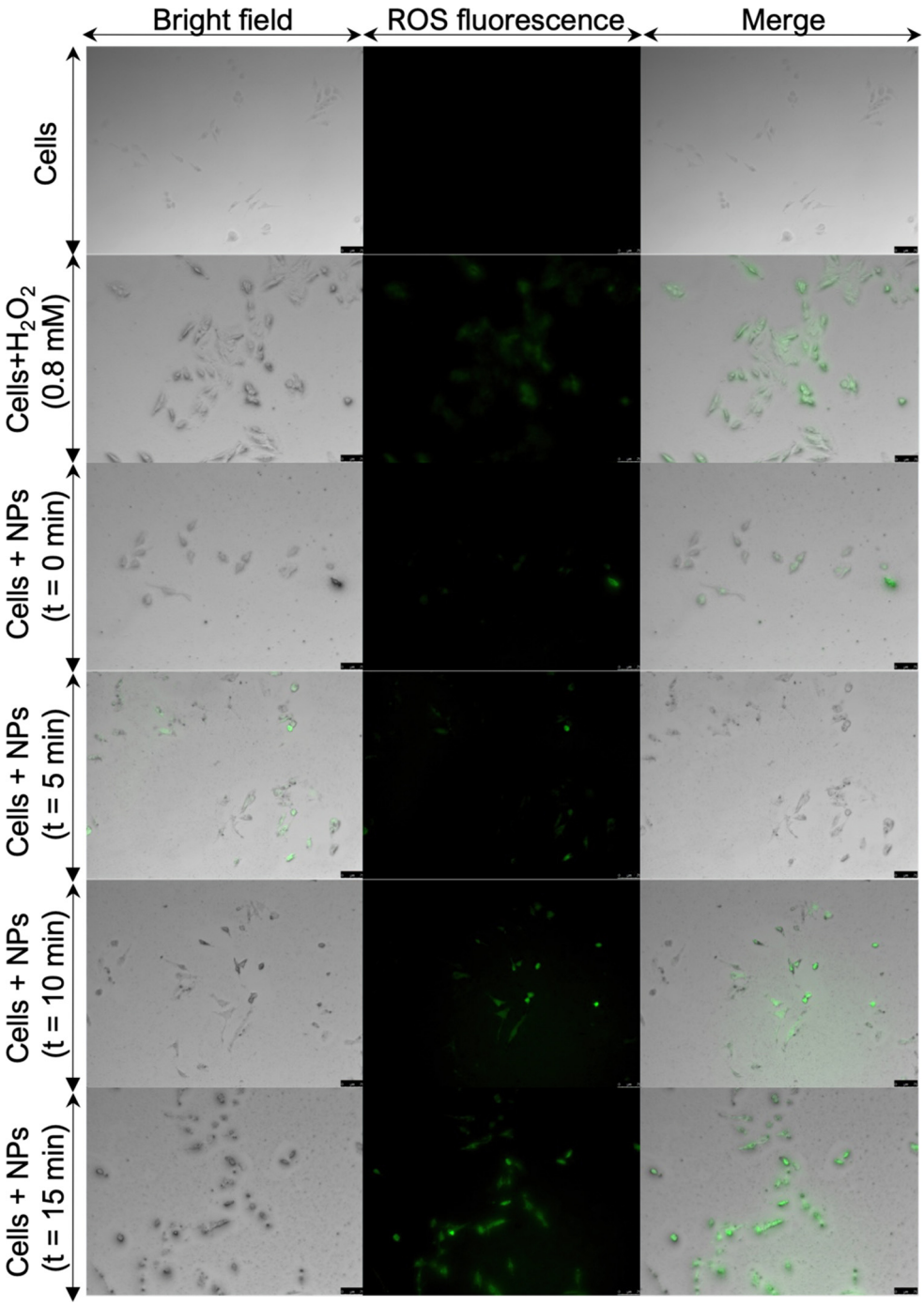

Fig. 5. Fluorescence microscopy images of ROS production by PSS/PLL-ICG/HA-coated AuNRs within HeLa cells under NIR irradiation with a 808 nm CW laser source (1.0 W/cm^2) for 15 min. Untreated cells were used as a negative control, whereas H_2O_2-treated cells were the positive one. Direct transmitted light (left), fluorescent green channel (middle, λ_{em} = 520 nm for detection kit) and merged images (right) are shown. Scale bars are 75 μm. (For interpretation of the references to color in this figure legend, the reader is referred to the web version of this article.)

noted when using, for example, gold nanoshells with ICG entrapped in their polymeric core, for which cell toxicities of ca. 70 and 80% were observed by combination of PPTT + PDT in the nanosystem in HeLa and MDA-MB-231 cancer cells under 2.0 W/cm^2 for 5 min [55]; in addition, Au nanostars encapsulated in $CaCO_3$ and functionalized with ICG were irradiated for 6 min at 1.0 W/cm^2, reaching cell toxicities of up to 92% at a particle concentration of 30 μg/mL [73]. In a similar approach, Au nanostars were functionalized with polyethylene glycol-5 kDa (PEG-5 kDa) and incorporated chlorin e-6, Ce6. Cell mortalities induced by the illumination of the nanoconstruct after 10 min at 2.0 W/cm^2 (NIR light of 671 nm) were from 15 to 95% in the dye concentration range from 0.25 to 4 μM [67].

Finally, further enhancements of cell toxicities were observed when increasing the irradiation time up to 10 min under illumination of 2.0 W/cm^2 (Fig. 7c). For PSS/PLL/HA-coated AuNRs, cell mortalities increased from ca. 7, 15 and 23% at 6 h to 47, 50 and 55% after 24 h of incubation at 4, 25 and 37 ^{0}C, respectively, whereas for PSS/PLL-ICG/HA-coated ones toxicities changed from ca. 3, 16, and 39% to ca. 58, 60 and 71% after 6 and 24 h of incubation at

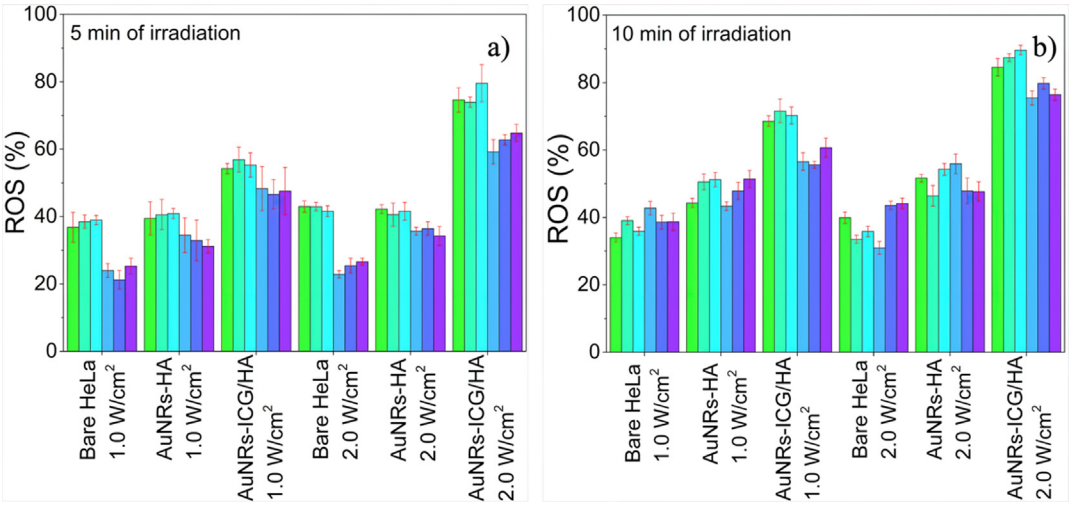

Fig. 6. ROS production induced by PSS/PLL-ICG/HA-coated AuNRs internalised within HeLa cells under NIR irradiation of 1.0 and 2.0 W/cm^2 with a 808 nm CW laser source for a period of (a) 5 min and (b) 10 min. Color bars denote the following conditions: 4 °C, 6 h of incubation; 25 °C, 6 h; 37 °C, 6 h; 4 °C, 24 h;, 25 °C, 24 h; 37 °C, 24 h. Untreated cells were used as a negative control whereas H_2O_2-treated cells were the positive one.

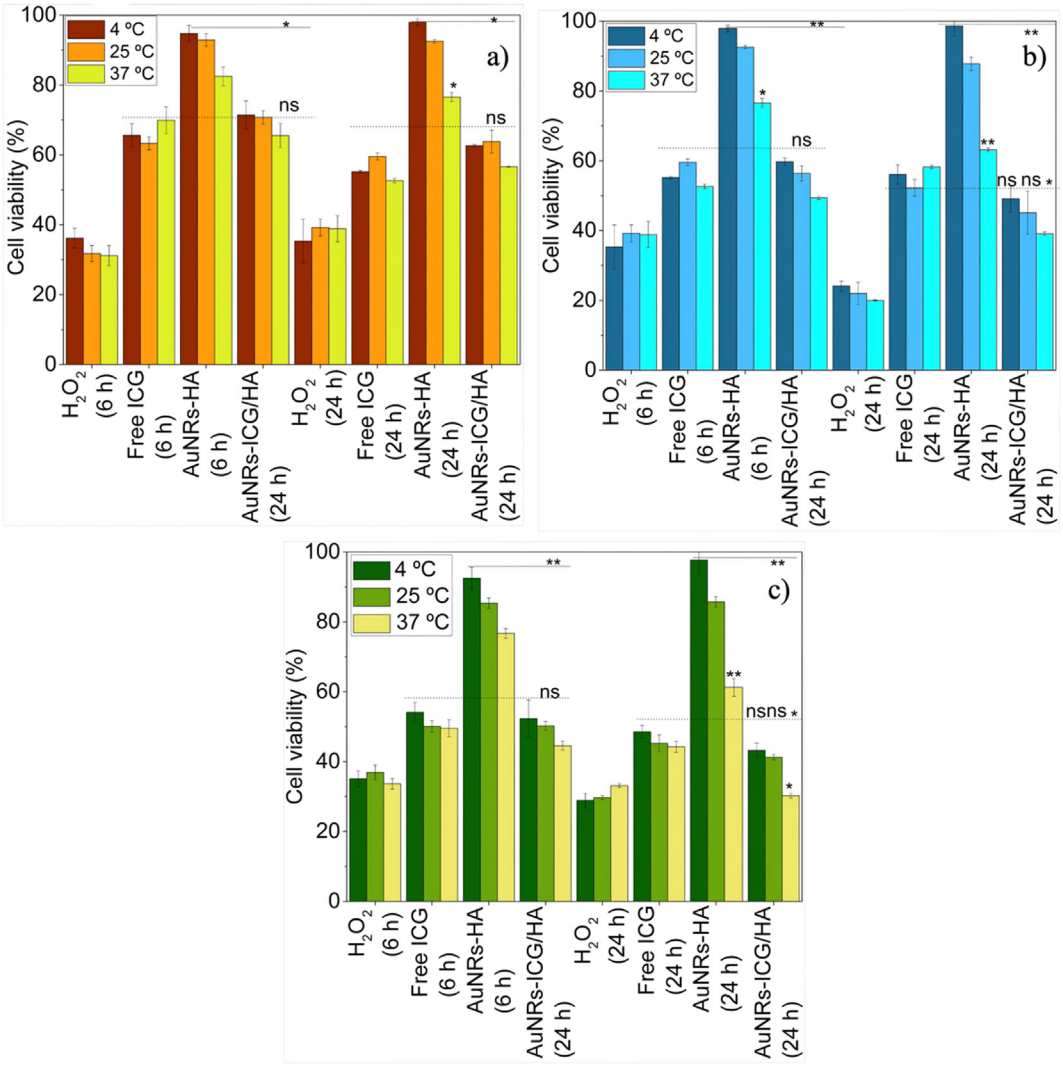

Fig. 7. Cell viabilities of HeLa cells after administration of PSS/PLL-ICG/HA-coated AuNRs and subsequent irradiation at a) 1.0 W/cm^2 for 5 min; b) 2.0 W/cm^2 for 5 min; and c) 2.0 W/cm^2 for 10 min at different temperatures and incubation times. Free and encapsulated ICG concentration was 22 μM whereas that of H_2O_2 was 0.8 mM (*P < 0.05; **P < 0.01; ns = not statistically significant).

Table 1
Relationship between external conditions and phototherapy-dominant cytotoxicity.

	Solution Temperature		
Fluence /Wcm^{-2}	4 °C	25 °C	37 °C
1.0 (t = 5 min)	PDT	PDT	PDT
2.0 (t = 5 min)	PDT	PDT	PDT + PTT
2.0 (t = 10 min)	PDT + PTT	PTT	PTT

the same solution temperatures, respectively. Thus, a larger exposure time to light irradiation seemed to enhance the photothermal effect whereas ROS generation seemed to be rather maintained after comparing the experimental data corresponding to PSS/PLL/HA-coated and PSS/PLL-ICG/HA-coated AuNRs. This behavior might arise from a lower contact of the dye with surrounding water molecules, which is key to generate $^1O_2$ and OH^- species, after its encapsulation within the polymeric coating. Direct contact of free ICG dye with water should facilitate both ROS generation and heat diffusion to the surroundings being reflected, in general, in slightly larger cell toxicities except at 37 ^{0}C after 24 h of incubation. Table 1 shows a brief summary indicating the main cytotoxic phototherapy as a function of the applied external conditions (fluence, irradiation time, temperature).

4. Conclusions

In this work, AuNRs were functionalized through the layer-by-layer technique to provide them with a biocompatible surface layer in which the NIR dye ICG was incorporated by means of its conjugation with the cationic biopolymer (PLL) used in the coating process. The obtained hybrid nanoplatform, to give PSS/PLL-ICG/HA-coated AuNRs, was able to provide a dual simultaneous PDT and PPTT therapy for tumor treatment thanks to the presence of ICG and the optical properties of AuNRs, which are favored by both the enhanced photostability of the dye and its location to large extents into the nanoconstruct even after extensive irradiation in contrast to previously developed nanosystems for similar purposes. In this regard, the dye release rates and profiles were observed to be perfectly controlled using both internal (e.g., enzymes as trypsin thanks to the degradability of PLL) or external (e.g., NIR light thanks to the optical properties of the dye itself and AuNRs) stimuli, if required. Surprisingly, the light to heat conversion provided by the PSS/PLL-ICG/HA-coated AuNRs nanoplatform was smaller compared to that of PSS/PLL/HA-coated AuNRs, that is, the platform without encapsulated dye. This behavior might originate from both the lower absorption cross section of the PS compared to the metallic core and competitive light absorption effects. The hybrid platform was also able to produce ROS species efficiently in test tube and intracellularly, and such generation depended on the fluence and time irradiation but not on the solution temperature [24,26,27]. Nevertheless, the protection of the dye inside the particle polymeric coating might hinder a more direct contact with oxygen-containing solvent, which may involve a slightly lower ROS production compared to the free dye at similar concentration and irradiation conditions. It was finally shown that the application of NIR light, particularly at 2.0 W/cm^2 and 37 °C, leads to important cell toxicity enhancements thanks to the simultaneous therapeutic outcomes provided by ROS and the photothermal effect, that is, by PDT and PPTT. However, it was observed that ROS toxic activity is predominant at lower fluencies (1.0 W/cm^2) and solution temperatures (4 and 25 °C) for which the macroscopic solution temperature increments are rather low; meanwhile, the cell toxic effect is enhanced by PPTT at longer irradiation times (10 min) and at 37 ^{0}C, for which the macroscopic temperature increments are above 45 °C. Temperature sensitization or thermal ablation regimes are achieved leading to either apoptosis or necrosis thermal-induced cell death pathways, respectively, which are added to the predominant PDT activity provided by the ICG dye. In this manner, we were able to decouple the contributions of PDT and PPTT to cell cytotoxicity as a function of solution temperature and irradiation conditions, which are many times obscure or directly not performed in similar studies, achieving a clear picture of how this nanoplatform can be more effective for its intended therapeutic application.

Funding

This research was funded by Agencia Estatal de Investigación (AEI), project number PID2019-109517RB-I00 and Xunta de Galicia ED431C 2022/18. ERDF funds are also acknowledged. A.C. also thanks Xunta de Galicia for grant number ED481D-2021–011. L. A. is grateful to CONACYT for funding her PhD fellowship.

Data Availability Statement

The data presented in this study are available on request from the corresponding authors.

Declaration of Competing Interest.

The authors declare that they have no known competing financial interests or personal relationships that could have appeared to influence the work reported in this paper.

CRediT authorship contribution statement

Lilia G. Arellano: Methodology, Validation, Formal analysis, Investigation, Data curation. **Eva M. Villar-Alvarez:** Methodology, Validation, Investigation. **Brenda Velasco:** Methodology, Validation. **Vicente Domínguez-Arca:** Software, Visualization. **Gerardo Prieto:** Writing – review & editing, Project administration. **Adriana Cambón:** Conceptualization, Data curation, Writing – original draft, Supervision, Funding acquisition. **Silvia Barbosa:** Conceptualization, Resources, Writing – original draft, Writing – review & editing, Supervision, Funding acquisition. **Pablo Taboada:** Conceptualization, Resources, Writing – review & editing, Project administration, Funding acquisition.

Data availability

Data will be made available on request.

Declaration of Competing Interest

The authors declare that they have no known competing financial interests or personal relationships that could have appeared to influence the work reported in this paper.

References

[1] X. Huang, M.A. El-Sayed, Plasmonic photo-thermal therapy (PPTT), Alexandria J. Medicine 47 (2011) 1–9, https://doi.org/10.1016/j.ajme.2011.01.001.
[2] H.S. Han, K.Y. Choi, Advances in Nanomaterial-Mediated Photothermal Cancer Therapies: Toward Clinical Applications, Biomedicines 9 (2021) 305, https://doi.org/10.3390/biomedicines9030305.
[3] Z. Zhang, J. Wang, C. Chen, Near-Infrared Light-Mediated Nanoplatforms for Cancer Thermo-Chemotherapy and Optical Imaging, Adv. Mater. 25 (2013) 3869–3880, https://doi.org/10.1002/adma.201301890.
[4] J. Fan, Y. Cheng, M. Sun, Functionalized Gold Nanoparticles: Synthesis Properties and Biomedical Applications, Chem. Records 20 (2020) 1474–1504, https://doi.org/10.1002/tcr.202000087.
[5] X. Huang, M.A. El-Sayed, Gold nanoparticles: Optical properties and implementations in cancer diagnosis and photothermal therapy, J. Adv. Res. 1 (2010) 13–28, https://doi.org/10.1016/j.jare.2010.02.002.

[6] J. Zheng, J., X. Cheng, H. Zhang, X. Bai, R. Ai, L. Shao, J. Wang, Gold Nanorods: The Most Versatile Plasmonic Nanoparticles. Chem. Rev. *121* (2021), 13342–13453, 10.1021/acs.chemrev.1c00422.
[7] M. Hu, J. Chen, Z.-Y. Li, L. Au, G.V. Hartland, X. Li, M. Marqueze, Y. Xia, Gold nanostructures: engineering their plasmonic properties for biomedical applications, Chem. Soc. *Rev.* 35 (1084–1094) (2006) 1084–1094, https://doi.org/10.1039/B517615H.
[8] G. von Maltzahn, J.H. Park, A. Agrawal, N.K. Bandaru, S.K. Das, M.J. Sailor, S.N. Bhatia, Computationally guided photothermal tumor therapy using long-circulating gold nanorod antennas, Cancer Res. 69 (2009) 3892–3900, https://doi.org/10.1158/0008-5472.Can-08-4242.
[9] M.L. Taylor, R.E. Wilson Jr., K.D. Amrhein, X. Huang, Gold Nanorod-Assisted Photothermal Therapy and Improvement Strategies, Bioengineering 9 (2022) 200, https://doi.org/10.3390/bioengineering9050200.
[10] C. Tomuleasa, O. Soritau, A. Orza, M. Dudea, B. Petrushev, O. Mosteanu, S. Susman, A. Florea, E. Pall, M. Aldea, G. Kacso, V. Cristea, I. Berindan-Neagoe, A. Irimie, Gold nanoparticles conjugated with cisplatin/doxorubicin/capecitabine lower the chemoresistance of hepatocellular carcinoma-derived cancer cells, J. Gastrointestinal Liver Dis. 21 (2012) 187–196.
[11] A. Wijaya, S.B. Schaffer, I.G. Pallares, K. Hamad-Schifferli, Selective Release of Multiple DNA Oligonucleotides from Gold Nanorods, ACS Nano 3 (2009) 80–86, https://doi.org/10.1021/nn800702n.
[12] J. He, X. Huang, Y.-C. Li, Y. Liu, T. Babu, M.A. Aronova, S. Wang, Z. Lu, X. Chen, Z. Nie, Self-Assembly of Amphiphilic Plasmonic Micelle-Like Nanoparticles in Selective Solvents, J. Am. Chem. Soc. 135 (2013) 7974–7984, https://doi.org/10.1021/ja402015s.
[13] X. Huang, I.H. El-Sayed, W. Qian, M.A. El-Sayed, Cancer Cell Imaging and Photothermal Therapy in the Near-Infrared Region by Using Gold Nanorods, J. Am. Chem. Soc. 128 (2006) 2115–2120, https://doi.org/10.1021/ja057254a.
[14] W.-S. Kuo, C.-N. Chang, Y.-T. Chang, M.-H. Yang, Y.-H. Chien, S.-J. Chen, C.-S. Yeh, Gold nanorods in photodynamic therapy, as hyperthermia agents, and in near-infrared optical imaging, Angew. Chem. Int. Ed. 49 (2010) 2711–2715, https://doi.org/10.1002/anie.200906927.
[15] B. Jang, J.-Y. Park, C.-H. Tung, I.-H. Kim, Y. Choi, Gold Nanorod−Photosensitizer Complex for Near-Infrared Fluorescence Imaging and Photodynamic/Photothermal Therapy In Vivo, ACS Nano 5 (2011) 1086–1094, https://doi.org/10.1021/nn102722z.
[16] Y. Mi, X. Liu, J. Zhao, J. Ding, S.-S. Feng, Multimodality treatment of cancer with herceptin conjugated, thermomagnetic iron oxides and docetaxel loaded nanoparticles of biodegradable polymers, Biomaterials 33 (2012) 7519–7529, https://doi.org/10.1016/j.biomaterials.2012.06.100.
[17] T.J. Dougherty, C.J. Gomer, B.W. Henderson, G. Jori, D. Kessel, M. Korbelik, J. Moan, Q. Peng, Photodynamic Therapy, J. Natl. Cancer Inst. 90 (1998) 889–905, https://doi.org/10.1093/jnci/90.12.889.
[18] M.T. Yaraki, M.B. Liu, Y.N. Tan, Emerging Strategies in Enhancing Singlet Oxygen Generation of Nano-Photosensitizers Toward Advanced Phototherapy, Nano-Micro Lett. 14 (2022) 135, https://doi.org/10.1007/s40820-022-00856-y.
[19] J.F. Lovell, T.W.B. Liu, J. Chen, G. Zheng, Activatable Photosensitizers for Imaging and Therapy, Chem. Rev. 110 (2010) 2839–2857, https://doi.org/10.1021/cr900236h.
[20] Z. Zhou, J. Song, L. Nie, X. Chen, Reactive oxygen species generating systems meeting challenges of photodynamic cancer therapy, Chem. Soc. Rev. 45 (2016) 6597–6626, https://doi.org/10.1039/c6cs00271d.
[21] T.P. Devasagayam, J.C. Tilak, K.K. Boloor, K.S. Sane, S.S. Ghaskadbi, R.D. Lele, Free radicals and antioxidants in human health: current status and future prospects, J. Association Physicians India 52 (2004) 794–804.
[22] S.B. Gibson, A matter of balance between life and death: targeting reactive oxygen species (ROS)-induced autophagy for cancer therapy, Autophagy 6 (2010) 835–837, https://doi.org/10.4161/auto.6.7.13335.
[23] J. Lin, S. Wang, P. Huang, Z. Wang, S. Chen, G. Niu, W. Li, J. He, D. Cui, G. Lu, X. Chen, Z. Nie, Photosensitizer-Loaded Gold Vesicles with Strong Plasmonic Coupling Effect for Imaging-Guided Photothermal/Photodynamic Therapy, ACS Nano 7 (2013) 5320–5329, https://doi.org/10.1021/nn4011686.
[24] J. Wang, M. You, G. Zhu, M.I. Shukoor, Z. Chen, Z. Zhao, M.B. Altman, Q. Yuan, Z. Zhu, Y. Chen, C.Z. Huang, W. Tan, Photosensitizer-gold nanorod composite for targeted multimodal therapy, Small 9 (2013) 3678–3684, https://doi.org/10.1002/smll.201202155.
[25] Z. Fan, C. Zhuang, S. Wang, Y. Zhang, Photodynamic and Photothermal Therapy of Hepatocellular Carcinoma, Front. Oncol. 11 (2021), https://doi.org/10.3389/fonc.2021.787780.
[26] J.Y. Kim, W.I. Choi, M. Kim, G. Tae, Tumor-targeting nanogel that can function independently for both photodynamic and photothermal therapy and its synergy from the procedure of PDT followed by PTT, J. Control. Release 171 (2013) 113–121, https://doi.org/10.1016/j.jconrel.2013.07.006.
[27] L. Wang, D. Meng, Y. Hao, Y. Zhao, D. Li, B. Zhang, Y. Zhang, Z. Zhang. Gold nanostars mediated combined photothermal and photodynamic therapy and X-ray imaging for cancer theranostic applications. J. Biomaterials Appl. *30* (20105) 547-557, 10.1177/0885328215594481.
[28] A. Kumar, S. Kumar, W.-K. Rhim, G.-H. Kim, J.-M. Nam, Oxidative Nanopeeling Chemistry-Based Synthesis and Photodynamic and Photothermal Therapeutic Applications of Plasmonic Core-Petal Nanostructures, J. Am. Chem. Soc. 136 (2014) 16317–16325, https://doi.org/10.1021/ja5085699.
[29] M. Dohadwala, J. Luo, L. Zhu, Y. Lin, G.J. Dougherty, S. Sharma, M. Huang, M. Pold, R.K. Batra, S.M. Dubinett, Non-small cell lung cancer cyclooxygenase-2-dependent invasion is mediated by CD44, J. Biol. Chem. 276 (2001) 20809–20812, https://doi.org/10.1074/jbc.C100140200.
[30] V.J. Wielenga, K.H. Heider, G.J. Offerhaus, G.R. Adolf, F.M. van den Berg, H. Ponta, P. Herrlich, S.T. Pals, Expression of CD44 variant proteins in human colorectal cancer is related to tumor progression, Cancer Res. 53 (1993) 4754–4756.
[31] Y. Watanabe, K. Kumon, Assessment by pulse dye-densitometry indocyanine green (ICG) clearance test of hepatic function of patients before cardiac surgery: Its value as a predictor of serious postoperative liver dysfunction, J. Cardiothor. Vasc. Anesth. 13 (1999) 299–303, https://doi.org/10.1016/S1053-0770(99)90267-7.
[32] T. Desmettre, T.J.M. Devoisselle, S. Mordon, Fluorescence properties and metabolic features of indocyanine green (ICG) as related to angiography, Survey Ophthal. 45 (2000) 15–27, https://doi.org/10.1016/s0039-6257(00)00123-5.
[33] D.E.J.G.J. Dolmans, D. Fukumura, R.K. Jain, Photodynamic therapy for cancer, Nature Rev. Cancer 3 (2003) 380–387, https://doi.org/10.1038/nrc1071.
[34] M.T. Jarvi, M.J. Niedre, M.S. Patterson, B.C. Wilson, Singlet oxygen luminescence dosimetry (SOLD) for photodynamic therapy: current status, challenges and future prospects, Photochem. Photobiol. 82 (2006) 1198–1210, https://doi.org/10.1562/2006-05-03-ir-891.
[35] R.R. Chance, A. Prock, R. Silbey, Molecular Fluorescence and Energy Transfer Near Interfaces, Adv. Chem. Phys. 37 (1978) 1–65, https://doi.org/10.1002/9780470142561.ch1.
[36] J. Gersten, A. Nitzan, Spectroscopic properties of molecules interacting with small dielectric particles, J. Chem. Phys. 75 (1981) 1139–1152, https://doi.org/10.1063/1.442161.
[37] J.L. Gersten, A. Nitzan, Accelerated energy transfer between molecules near a solid particle, Chem. Phys. Lett. 104 (1984) 31–37, https://doi.org/10.1016/0009-2614(84)85300-2.
[38] B. P. George, A. Chota, P. Sarbadhikary, H.Abrahamse. Fundamentals and applications of metal nanoparticle- enhanced singlet oxygen generation for improved cancer photodynamic therapy.Front Chem. *10* (2022) 964674, 10.3389/fchem.2022.964674.
[39] R. Khursheed, K. Dua, S. Vishwas, M. Gulati, N.K. Jha, G.M. Aldhafeeri, F.G. Alanazi, B.H. Goh, G. Gupta, K.R. Paudel, P.M. Hansbro, D.K. Chellappan, S.K. Singh, Biomedical applications of metallic nanoparticles in cancer: Current status and future perspectives, Biomed. Pharmacother. 150 (2022), https://doi.org/10.1016/j.biopha.2022.112951.
[40] S.W. Provencher, P. Štěpánek, Global Analysis of Dynamic Light Scattering Autocorrelation Functions, Part. Part. Synth. Charat. 13 (1996) 291–294, https://doi.org/10.1002/ppsc.19960130507.
[41] C.S. Jin, J.F. Lovell, J. Chen, G. Zheng, Ablation of hypoxic tumors with dose-equivalent photothermal, but not photodynamic, therapy using a nanostructured porphyrin assembly, ACS Nano 7 (2013) 2541–2550, https://doi.org/10.1021/nn3058642.
[42] S.M. Ranuncolo, V. Ladeda, S. Specterman, M. Varela, J. Lastiri, A. Morandi, E. Matos, E.B. de Kier Joffé, L. Puricelli, M.G. Pallotta, CD44 expression in human gliomas, J. Surg. Oncol. 79 (2022) 30–36, https://doi.org/10.1002/jso.10045.
[43] H.S.S. Qhattal, X. Liu, Characterization of CD44-Mediated Cancer Cell Uptake and Intracellular Distribution of Hyaluronan-Grafted Liposomes, Mol. Pharm. 8 (2011) 1233–1246, https://doi.org/10.1021/mp2000428.
[44] J. Pérez-Juste, I. Pastoriza-Santosa, L.M. Liz-Marzána, P. Mulvaney, Gold nanorods: Synthesis, characterization and applications, Coord. Chem. Rev. 249 (2005) 1870–1901, https://doi.org/10.1016/j.ccr.2005.01.030.
[45] C. Yu, J. Irudayaraj, Quantitative Evaluation of Sensitivity and Selectivity of Multiplex NanoSPR Biosensor Assays, Biophys. J. 93 (2007) 3684–3692, https://doi.org/10.1529/biophysj.107.110064.
[46] P. Kekicheff, O. Spalla, Refractive Index of Thin Aqueous Films Confined between Two Hydrophobic Surfaces, Langmuir 10 (1994) 1584–1591, https://doi.org/10.1021/la00017a043.
[47] K. Urbanska et al., Indocyanine green as a prospective sensitizer for photodynamic therapy of melanomas, Acta Biochim. Polonica 49 (2) (2002) 387–391.
[48] S.E.A. Gratton, P.A. Ropp, P.D. Pohlhaus, J.M. DeSimone, The effect of particle design on cellular internalization pathways, Proc. Natl. Acad. Sci. USA 105 (2008) 11613–11618, https://doi.org/10.1073/pnas.0801763105.
[49] I.J. Fox, E.H. Wood, Indocyanine green: physical and physiologic properties, Proc. Staff Meetings Mayo Clinic 35 (1960) 732–744.
[50] O.G. Björnsson, R. Murphy, V.S. Chadwick, S. Björnsson, Physiochemical studies on indocyanine green: molar lineic absorbance, pH tolerance, activation energy and rate of decay in various solvents, J. Clin. Chem. Clin. Biochem. 21 (1983) 453–458, https://doi.org/10.1515/cclm.1983.21.7.453.
[51] W.F. Sutterer, S.E. Hardin, W. Benson, L.J. Krovetz, G.L. Schiebler, Optical behavior of indocyanine green dye in blood and in aqueous solution, Am. Heart J. 72 (1966) 345–350, https://doi.org/10.1016/S0002-8703(66)80008-X.
[52] H. Passing, A. Bablok, A new biometrical procedure for testing the equality of measurements from two different analytical methods. Application of linear regression procedures for method comparison studies in clinical chemistry, Part I, J Clin. Chem. 21 (1983) 709–720, https://doi.org/10.1515/cclm.1983.21.11.709.
[53] J. Gathje, R.R. Steuer, K.R. Nicholes, Stability studies on indocyanine green dye, J. Appl. Physiol. 29 (1970) 181–185, https://doi.org/10.1152/jappl.1970.29.2.181.
[54] M.L. Landsman, G. Kwant, G.A. Mook, W.G. Zijlstra, Light-absorbing properties, stability, and spectral stabilization of indocyanine green, J. Appl. Pphysiol. 40 (1976) 575–583, https://doi.org/10.1152/jappl.1976.40.4.575.

[55] A. Topete, M. Alatorre-Meda, P. Iglesias, E.M. Villar-Alvarez, S. Barbosa, J.A. Costoya, P. Taboada, V. Mosquera, Fluorescent Drug-Loaded, Polymeric-Based, Branched Gold Nanoshells for Localized Multimodal Therapy and Imaging of Tumoral Cells, ACS Nano 8 (2014) 2725–2738, https://doi.org/10.1021/nn406425h.
[56] L. C. Smith, V. Edwards, C. Tung, M. J. Logan, M. S. Wadhwa, J. Duguid, L. C. Smith Synthetic peptide-based DNA complexes for nonviral gene delivery. Adv. Drug Deliv. Rev. *30* (1998) 115-131, 10.1016/s0169-409x(97)00111-7.
[57] G. Shafirstein, W. Bäumler, L.J. Hennings, E.R. Siegel, R. Friedman, M.A. Moreno, J. Webber, C. Jackson, R.J. Griffin, Indocyanine green enhanced near-infrared laser treatment of murine mammary carcinoma, Int. J. Cancer 130 (2012) 1208–1215, https://doi.org/10.1002/ijc.26126.
[58] R. Philip, A. Penzkofera, W. Bäumlerb, R.M. Szeimies, C. Abels, Absorption and fluorescence spectroscopic investigation of indocyanine green, J. Photochem. Photobiol. A: Chemistry 96 (1996) 137–148, https://doi.org/10.1016/1010-6030(95)04292-X.
[59] W. Bäumler, C. Abels, S. Karrer, T. Weiß, H. Messmann, M. Landthaler, R.-M. Szeimies, Photo-oxidative killing of human colonic cancer cells using indocyanine green and infrared light, British J. Cancer. 80 (1999) 360–363, https://doi.org/10.1038/sj.bjc.6690363.
[60] E. Reichel, C.A. Puliafito, J.S. Duker, D.R. Guyer, Indocyanine green dye-enhanced diode laser photocoagulation of poorly defined subfoveal choroidal neovascularization, Ophthalmic Surg. 25 (1994) 195–201.
[61] E. Engel, R. Schraml, T. Maisch, K. Kobuch, B. König, R.-M. Szeimies, J. Hillenkamp, W. Bäumler, R. Vasold, Light-induced decomposition of indocyanine green, Invest. Ophthalmol. Vis. Sci. 49 (2008) 1777–1783, https://doi.org/10.1167/iovs.07-0911.
[62] M. Pérez-Hernández, P. Del Pino, S.G. Mitchell, M. Moros, G. Stepien, B. Pelaz, W.J. Parak, E.M. Gálvez, J. Pardo, J.M. de la Fuente, Dissecting and molecular mechanisms of apoptosis during the photothermal therapy using gold nanoprismsm, ACS Nano 9 (2015) 52–61, https://doi.org/10.1021/nn505468v.
[63] A.M. Alkilany, L.B. Thompson, S.P. Boulos, P.N. Sisco, C.J. Murphy, Gold nanorods: Their potential for photothermal therapeutics and drug delivery, tempered by the complexity of their biological interactions, Adv. Drug Deliv. Rev. 64 (2012) 190–199, https://doi.org/10.1016/j.addr.2011.03.005.
[64] P.K. Jain, K.S. Lee, I.H. El-Sayed, M.A. El-Sayed, Calculated Absorption and Scattering Properties of Gold Nanoparticles of Different Size, Shape, and Composition: Applications in Biological Imaging and Biomedicine, J. Phys. Chem. B 110 (2006) 7238–7248, https://doi.org/10.1021/jp057170o.
[65] R. Huschka, J. Zuloaga, M.W. Knigh, L.V. Brown, P. Nordlander, N.J. Halas, Light-Induced Release of DNA from Gold Nanoparticles: Nanoshells and Nanorods, J. Am. Chem. Soc. 133 (2011) 12247–12255, https://doi.org/10.1021/ja204578e.
[66] K.R. Weishaupt, C.J. Gomer, T.J. Dougherty, Identification of singlet oxygen as the cytotoxic agent in photoinactivation of a murine tumor, Cancer Res. 36 (1976) 2326–2329.
[67] S. Wang, P. Huang, L. Nie, R. Xing, D. Liu, Z. Wang, J. Lin, S. Chen, G. Niu, G. Lu, X. Chen, Single Continuous Wave Laser Induced Photodynamic/Plasmonic Photothermal Therapy Using Photosensitizer-Functionalized Gold Nanostars, Adv. Mater. 25 (2013) 3055–3061, https://doi.org/10.1002/adma.201204623.
[68] B. Tian, C. Wang, S. Zhang, L. Feng, Z. Liu, Photothermally Enhanced Photodynamic Therapy Delivered by Nano-Graphene Oxide, ACS Nano 5 (2011) 7000–7009, https://doi.org/10.1021/nn201560b.
[69] J.A. Howard, G.D. Mendenhall, Autoxidation and Photooxidation of 1,3-Diphenylisobenzofuran: A Kinetic and Product Study, Can J. Chem. 53 (1975) 2199–2201, https://doi.org/10.1139/v75-307.
[70] J.-M. Aubry, C. Pierlot, J. Rigaudy, R. Schmidt, Reversible Binding of Oxygen to Aromatic Compounds, Acc. Chem. Res. 36 (2003) 668–675, https://doi.org/10.1021/ar010086g.
[71] A. Sivéry, F. Anquez, C. Pierlot, J.M. Aubry, E. Courtade, Singlet oxygen ($^1O_2$) generation upon 1270 nm laser irradiation of ground state oxygen ($^3O_2$) dissolved in organic solvents: Simultaneous and independent determination of $^1O_2$ production rate and reactivity with chemical traps, Chem. Phys. Lett. 555 (2013) 252–257, https://doi.org/10.1016/j.cplett.2012.10.063.
[72] Y. Zhang, X. Zhan, J. Xiong, S. Peng, W. Huang, R. Joshi, Y. Cai, Y. Liu, R. Li, K. Yuan, N. Zhou, W. Min, Temperature-dependent cell death patterns induced by functionalized gold nanoparticle photothermal therapy in melanoma cells, Sci. Rep. 8 (2018) 8720, https://doi.org/10.1038/s41598-018-26978-1.
[73] Y. Liu, X. Zhi, M. Yang, J. Zhang, L. Lin, X. Zhao, W. Hou, C. Zhang, Q. Zhang, F. Pan, G. Alfranca, Y. Yang, J.M. de la Fuente, J. Ni, D. Cui, Tumor-triggered drug release from calcium carbonate-encapsulated gold nanostars for near-infrared photodynamic/photothermal combination antitumor therapy, Theranostics 7 (2017) 1650–1662, https://doi.org/10.7150/thno.17602.